ACS APPLIED MATERIALS & INTERFACES

Research Article

Cite This: ACS Appl. Mater. Interfaces 2017, 9, 35757-35774

www.acsami.org

Morphological Control of Mesoporosity and Nanoparticles within Co_3O_4–CuO Electrospun Nanofibers: Quantum Confinement and Visible Light Photocatalysis Performance

Amaresh C Pradhan* and Tamer Uyar*

Institute of Materials Science & Nanotechnology, UNAM-National Nanotechnology Research Center, Bilkent University, Ankara, 06800, Turkey

Supporting Information

ABSTRACT: The one-dimensional (1D) mesoporous and interconnected nanoparticles (NPs) enriched composite Co_3O_4–CuO nanofibers (NFs) in the ratio Co:Cu = 1/4 (Co_3O_4–CuO NFs) composite have been synthesized by electrospinning and calcination of mixed polymeric template. Not merely the mesoporous composite Co_3O_4–CuO NFs but also single mesoporous Co_3O_4 NFs and CuO NFs have been produced for comparison. The choice of mixed polymer templates such as polyvinylpyrrolidone (PVP) and polyethylene glycol (PEG) for electrospinning is responsible for the formation of 1D mesoporous NFs. The HR-TEM result showed evolution of interconnected nanoparticles (NPs) and creation of mesoporosity in all electrospun NFs. The quantum confinement is due to NPs within NFs and has been proved by the surface-enhanced Raman scattering (SERS) study and the UV–vis–NRI diffuse reflectance spectra (DRS). The high intense photoluminescence (PL) spectra showing blue shift of all NFs also confirmed the quantum confinement phenomena. The lowering of PL spectrum after mixing of CuO in Co_3O_4 nanofibers framework (Co_3O_4–CuO NFs) proved CuO as an efficient visible light response low cost cocatalyst/charge separator. The red shifting of the band gap in composite Co_3O_4–CuO NFs is due to the internal charge transfer between Co^{2+} to Co^{3+} and Cu^{2+}, proved by UV–vis absorption spectroscopy. Creation of oxygen vacancies by mixing of CuO and Co_3O_4 also prevents the electron–hole recombination and enhances the photocatalytic activity in composite Co_3O_4–CuO NFs. The photocurrent density, Mott–Schottky (MS), and electrochemical impedance spectroscopy (EIS) studies of all NFs favor the high photocatalytic performance. The mesoporous composite Co_3O_4–CuO NFs exhibits high photocatalytic activity toward phenolic compounds degradation as compared to the other two NFs (Co_3O_4 NFs and CuO NFs). The kinetic study of phenolic compounds followed first order rate equation. The high photocatalytic activity of composite Co_3O_4–CuO NFs is attributed to the formation of mesoporosity and interconnected NPs within NFs framework, quantum confinement, extended light absorption property, internal charge transfer, and effective photogenerated charge separations.

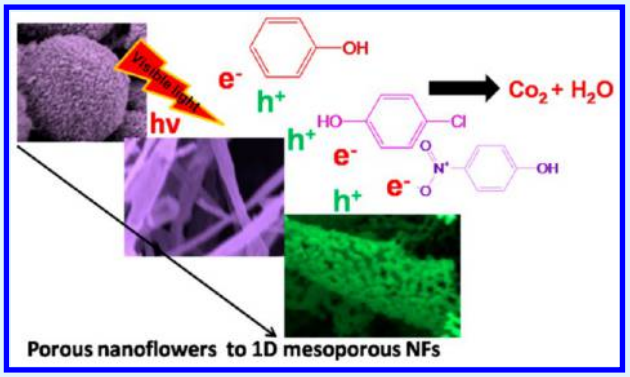

KEYWORDS: *electrospinning, nanofibers, quantum confinement, mesoporous, phenolic compounds, visible light*

1. INTRODUCTION

Semiconductor photocatalysis, a promising green technology, has attracted significant attention because of its high performance in environmental pollution control.[1,2] Phenolic compounds are toxic organic byproducts produced during the manufacturing process of agrochemicals, dyes, and pharmaceuticals.[3,4] Most of these compounds have been listed as toxic priority pollutants by the European community and U.S. (Environmental Protection Agency).[5] Nanostructured materials, especially metal and metal oxide nanoparticles, nanoplates, nanorods, nanotubes, and nanofibers, have attracted particular interest in catalytic applications because of their unique optical properties, versatile catalytic activities, and high surface areas.[6−8] Among them, one-dimensional (1D) structures have a great deal of attention due to their superior charge transport properties, few grain boundaries, and the quick ion diffusion at the semiconductor–phenolic compounds solutions interface.[9,10] 1D nanostructures such as metal oxide nanofibers (NFs) by electrospinning have remarkable characteristics, e.g., high porosity, a large surface area to volume ratio, and excellent substrates for secondary nanostructures.[11,12] The metal oxide Co_3O_4 is a visible light active p-type semiconductor (1.48 eV) with attractive electronic and structural properties.[13] But bulk Co_3O_4 has limitation in photocatalytic activity. In order to make Co_3O_4 an effective photocatalyst, it is a necessary to make a heterojunction with other semiconductor, resulting in

Received: June 23, 2017
Accepted: September 26, 2017
Published: September 26, 2017

DOI: 10.1021/acsami.7b09026
ACS Appl. Mater. Interfaces 2017, 9, 35757–35774

enhanced photocatalytic activity due to lowering of electron−hole recombination.[14,15] Hence, mixture of Co_3O_4 with other semiconductor oxides could fulfill the electron−hole separation strategy. The other strategy is morphology and structural framework of Co_3O_4. Recently, Co_3O_4 nanofibers fabricated from spiral electrospinning have been utilized as a catalyst for the oxidation of formaldehyde.[16] The best option is to choose semiconductor oxides having cocatalyst property. A cocatalyst can enhance the photocatalytic activity of a semiconductor by (i) suppressing the electron−hole recombination by trapping the photogenerated electrons, (ii) improving the photostability of the catalyst by consumption of photogenerated charges, particularly holes, and (iii) lowering the activation energy and hence catalyzing the reactions.[17] Transition metal oxide semiconductor CuO (1.2 eV) has been reported as cocatalyst to enhance the photocatalytic activity. Shah et al. observed high photocatalytic activity of Ag/AgCl/TiO_2 by using CuO as cocatalyst.[18] Photodegradation activity of organic substance by WO_3 has been enhanced by using CuO as cocatalyst.[19] Hence, design and combination of semiconductor Co_3O_4 and semiconductor CuO cocatalyst NFs could improve the visible light photocatalytic performance. The design and mixed modification of Co_3O_4 and CuO include (i) morphological modification such as mesoporosity and NPs within NFs, (ii) quantum confinement effect, and (iii) combination of reactive facets of two oxides NFs.

Construction of mesoporous structure within NFs can also enhance the photocatalytic performance.[16] The construction of mesoporous structures in single Co_3O_4 and CuO and in mixture of both can elevate the surface area of the photocatalyst which results in the increase of a large number of reactive sites. It can also enhance the light absorption efficiency because of more photons being distributed onto the surface of the photocatalyst, using the pores as light transfer paths.[20] Moreover, mesoporous materials themselves can be used as a support of guest materials.[21] The surface texture of Co_3O_4, CuO, and mixture of both NFs can be constructed by adopting electrospinning process. It has been noted the electrospinning process aids the creation of porous and well-ordered NFs by adding suitable optimized block copolymer template and other additives like acid and appropriate solvent.[22,23] Hence, mixing of polyvinylpyrrolidone (PVP) and polyethylene glycol (PEG) solutions as mixed polymeric template may fulfill the porous NFs/porous NPs within NFs strategy. The vital benefit of electrospinning process is the formation of surface hydroxyl (−OH), which also plays a significant role in its photocatalytic activity.[24]

Hence, formation of mesoporosity within the composite Co_3O_4−CuO NFs could enhance the surface reactive sites and light absorption property. Furthermore, quantum confinement effects generated from quantum dots have been investigated intensively.[25] When the crystal size of the semiconductor is close to its exciton Bohr radius, its band gap will be enlarged while the crystal size is decreased.[25] So formation of NPs within NFs could provide the quantum confinement phenomena and will lead to enhanced light absorption property. Moreover, the combination of reactive facets of Co_3O_4 and CuO NFs can act as an efficient composite photocatalysts for phenolic compound degradation. It has been noted that the mesoporous Co_3O_4 exposed {110} facets showed high activity in oxidation of ethylene.[26] Xie et al.[27] observed that the Co_3O_4 nanorods, which predominantly exposed their {110} facets, favoring the presence of active Co^{3+} species at the surface, exhibited a much higher activity for CO oxidation. Therefore, the synthesis design of nanostructured Co_3O_4 catalysts with highly reactive crystal facets is a key to exploring different catalytic properties and applications. Thus, fabrication of porous NFs could be the better option for the generation of highly reactive {110} facets. Not merely Co_3O_4 facets but also CuO exposed with {001} facets have high reactive sites for gas sensing and Li-ion battery application.[28] So combination of both mesoporous Co_3O_4 and CuO NFs with their respective reactive facets could enhance the photocatalytic properties.

In this article, we report the practical approach for the fabrication of mesoporous Co_3O_4 NFs, CuO NFs, and composite Co_3O_4−CuO NFs by in situ electrospinning process. The mixed polymeric templates (PVP and PEG) have taken the key role for the fabrication of above-mentioned electrospun mesoporous NFs (Co_3O_4 NFs, CuO NFs) and Co_3O_4−CuO composite NFs. Here, we have explored the mechanistic pathways for the formation of mesoporous and NPs within all fabricated electrospun NFs. It is investigated that the quantum confinement effect arises due to the formation of NPs within NFs, proved by SERS analyses. We have also explored the mechanism of the photocatalytic phenolic compound degradation process and the quantum confinement induced visible light photocatalytic activity of mesoporous composite Co_3O_4−CuO NFs. In the present study, it is also explained that the role of CuO is as a cocatalyst which enhanced the photocatalytic activity in the composite Co_3O_4−CuO NFs by separation of charge carriers and suppress their recombination. Under the combined action of Co_3O_4 and CuO, the as-synthesized mesoporous composite Co_3O_4−CuO NFs exhibits the highest photocatalytic activity compared with the other two single mesporous NFs. This is explained by the enhanced morphology, textural property, and optical properties.

2. EXPERIMENTAL SECTION

2.1. Materials. All the chemicals and reagents are of analytical grade and used without further purification. Cu(II) acetate (98%, Aldrich), Co(II) acetate (98%, Aldrich), polyethylene glycol(PEG, Mw = 1000 g/mol, Sigma-Aldrich), polyvinylpyrrolidone (PVP, Mw = 1 300 000 g/mol, Aldrich), isopropanol (95.5%, Sigma-Aldrich), acetic acid (100%, Sigma), 4-chlorophenol (99%, Alfa Aesar), 4-nitrophenol (99%, Alfa Aesar), phenol (99%, Alfa Aesar), nitric acid (Sigma), ammonia (Sigma), rhodamine 6G (98%, Sigma), potassium iodide (98%, Aldrich), and *p*-benzoquinone (98.5%, Alfa Aesar) were used in the present study.

2.2. Electrospinning of Mesoporous CuO NFs, CuO NFs, and Porous CuO Nanoflower. In order to optimize the mesoporous CuO NFs strategy, the Cu(II) acetate was taken as precursor of CuO. The experimental procedure proceeded by taking 0.5 g of Cu(II) acetate dissolved into the mixture of 1 g of PVP and 0.5 g of PEG (PVP:PEG = 3:1) in 10 mL of isopropanol. The reaction solution was stabilized by adding 1 mL of acetic acid. The whole solution was stirred for 24 h prior to electrospinning. Further, the solution was filled in a 3 mL plastic syringe with needle diameter of 0.4 mm and placed on a syringe pump (KDS101, KD Scientific, USA). The flow rate of the polymer solution was controlled by the syringe pump at fixed rate of 0.5 mL h^{-1}. The electric field (15 kV) was applied from a high voltage power supply (Spellman, SL series, USA). The sample was collected on aluminum foil which was grounded by metal collector at a distance 17 cm from the needle tip. Electrospinning procedure was carried out at 23 °C and 18% relative humidity in a Plexiglas box. Finally, the mesoporous CuO NFs were fabricated by calcining the PVP/CuO/PEG composite nanofibers at 450 °C for 4 h in air. The materials and the representative SEM images are summarized in the Scheme 1. Similarly, CuO NFs were prepared by taking only PVP as polymer template. The other parameters like concentration of

DOI: 10.1021/acsami.7b09026
ACS Appl. Mater. Interfaces 2017, 9, 35757−35774

Scheme 1. Electrosprayed Porous CuO Nanoflowers (Polymeric Matrix, PEG Only), Electrospun CuO NFs (Polymeric Matrix, PVP Only), and Mesoporous CuO NFs (Polymeric Matrix, PEG/PVP Mixture) Obtained after Calcination at 450 °C for 4 h

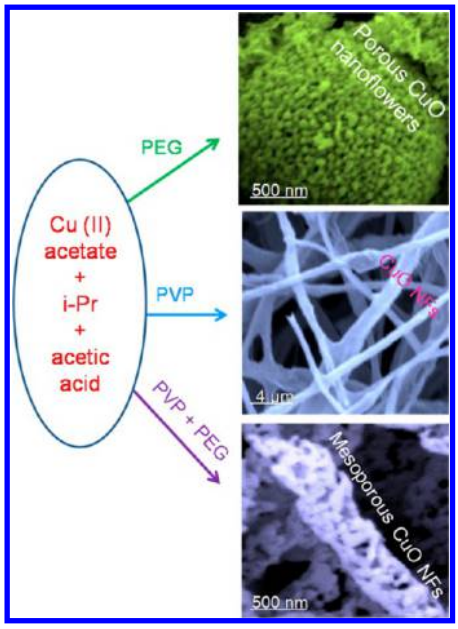

isopropanol, acetic acid and amount of Cu(II) acetate were similar to those of mesoporous CuO NFs. The CuO NFs were prepared by calcining PVP/CuO at 450 °C for 4 h. Moreover the porous CuO nanoflowers were prepared only by using the PEG as a polymeric template. Since PEG is a low molecular weight matrix, electrospraying was occurred instead of electrospinning in which particles were formed instead of fibers. The concentrations of isopropanol, acetic acid, and amount Cu precursor were similar to those for mesoporous CuO NFs and CuO NFs. Finally, porous CuO nanoflowers were produced by calcining PEG/CuO at 450 °C for 4 h (Scheme 1). Thus, it was understood that the mixture of PVP and PEG was responsible for the formation of mesoporous CuO NFs whereas the use of only PVP and PEG yielded the formation of CuO NFs, and porous CuO nanoflowers, respectively. In order to adopt the mesoporous NFs strategy, the other oxides such as mesoporous Co_3O_4 NFs and mesoporous composite Co_3O_4–CuO NFs have been prepared by using the mixture of PVP/PEG matrix, and the details are given in the following section.

2.3. Electrospinning of Mesoporous Co_3O_4 NFs and Mesoporous Composite Co_3O_4–CuO NFs. For the synthesis of mesoporous Co_3O_4 NFs and mesoporous composite Co_3O_4–CuO NFs, the optimal conditions/parameters were applied, like the electrospinning of mesoporous CuO NFs, i.e., using mixed PVP/PEG polymeric matrix. The mesoporous Co_3O_4 NFs are fabricated by taking 0.5 g of cobalt(II) acetate as a precursor. The synthesis process was followed in a similar way as mesoporous CuO NFs. Finally, the Co_3O_4 NFs were formed by calcined the PVP/Co_3O_4/PEG composite at 450 °C for 4 h in air. The mesoporous composite Co_3O_4–CuO NFs were fabricated by electrospinning method by taking a mixture of Co(II) acetate and Cu(II) acetate as a precursor, respectively. Composite Co_3O_4–CuO NFs (Co:Cu = 1/4) were synthesized by taking a calculated amount of Co(II) and Cu(II) acetate in the mixture of PVP:PEG = 3:1, in isopropanol and acetic acid. The whole solution was stirred for 24 h before electrospinning. Lastly, the mesoporous composite Co_3O_4–CuO NFs were fabricated by the calcinations of PVP/Co_3O_4–CuO/PEG composite at 450 °C for 4 h in air. The mesoporous composite Co_3O_4–CuO NFs in the ratio Co:Cu = 1/4 are denoted as Co_3O_4–CuO NFs. In a similar way, Co_3O_4–CuO NFs (Co:Cu = 1/3) and Co_3O_4–CuO NFs (Co:Cu = 1/2) have been synthesized for comparison of photocatalytic performance.

2.4. Characterization. The specific surface area, pore size, and pore volume of mesoporous NFs were measured by N_2 sorption method at liquid nitrogen temperature (−196 °C) using Quantachrome Instrument Autosorb (iQ_2). The specific surface area and pore size distribution were estimated based on Brunauer–Emmett–Teller (BET) and Barrett–Joyner– Halenda (BJH) methods, respectively. The crystal structures of the nanofibers were characterized using a PANalyticalX'Pert Pro multipurpose X-ray diffractometer (XRD) in the range of 2θ = 10–80° with Cu Kα (1.5418 Å) radiation. The surface morphology and elemental composition of mesoporous NFs were analyzed by field emission scanning electron microscopy (FE-SEM, Quanta 200 FEG, FEI). The morphology and mesoporosity of the nanofibers were examined by high resolution transmission electron microscope (HRTEM, Tecnai G2 F30, FEI). The scanning transmission electron microscopy–energy dispersive X-ray (STEM-EDX) analysis was used to study composition of the metal oxides within the nanofibers. The diameter of the NFs was calculated by ImageJ software. The UV–vis absorption spectra of the mesoporous NFs were recorded by UV–vis spectrophotometer (Varian Cary 100). The UV–visible–near-infrared diffuse reflectance spectra (UV–vis–NIR DRS) of the NFs were recorded by UV–vis–NIR spectrophotometer (Cary 5000). The photoluminescence spectra were measured on a fluorescence spectrometer (FL-1057 TCSPC) with an excitation wavelength at 390 nm light. Raman spectra measurement was conducted on a scanning near-field optical spectroscopy (SNOM) confocal Raman spectroscope (WITec) with a laser light wavelength of 532 nm. The Fourier transform infrared (FTIR) spectra of the samples were recorded with a Bruker VERTEX 70 in the range of 400–4000 cm^{-1} at room temperature using KBr pellet.

2.5. Visible Light Photocatalytic Degradation of Phenolic Compounds. The visible light photocatalytic degradation of phenolic compounds was examined by taking phenol, 4-chlorophenol (4-CP), and 4-nitrophenol (4-NP) solution. A stock solution of 20 mg L^{-1} for phenol, 4-CP, and 4-NP was prepared and suitably aqueous diluted to the required initial concentration. Prior to photocatalysis, the phenolic compounds solution was stirred for 20 min in order to reach equilibrium. Photocatalytic degradation of phenolic compounds (phenol, 4-CP, and 4-NP) was carried out by taking 10 mL of each solution (20 mg L^{-1}), 1 mg·mL^{-1} of catalyst dose at pH 6 for 70 min. The pH of the solution was monitored by Mettler Toledo pH meter with proper addition of 0.01 M HNO_3 and/or NH_4OH. The phenolic compounds solution with catalyst was placed for visible light irradiation (300 W, Osram, sunlight simulation)) at room temperature. The separated reaction solution from catalyst was analyzed UV–vis spectrophotometer (Varian Cary 100). The maximum absorbance of phenol, 4-CP, and 4-NP were at 210, 224, and 316 nm, respectively.

2.6. Surface-Enhanced Raman Spectroscopy. For surface-enhance Raman spectroscopy (SERS) measurements,[29] 500 μL of Rh 6G water solution of 20 μM was kept under ultrasound with 1 mg of all respective NFs. Then the Rh 6G-absorbed NFs were dispersed in 50 μL of water. The suspension of 10 μL was dropped onto a glass slide. The dropped solution spread evenly into a circle. After evaporation of the water, the sample was subjected to Raman measurement. All experiments were carried out at room temperature in the same conditions.

2.7. Active Species Trapping Experiments. The holes and radicals trapping experiments were conducted by adding various scavengers to the mesoporous composite Co_3O_4–CuO NFs in order to know the main reactive radical species involved in the photocatalytic process. Three different scavengers such as potassium iodide (KI; 0.1 mmol), isopropyl alcohol (IPA; 0.1 mmol), and *p*-benzoquinone (BQ; 0.1 mmol) have been used for the detection of holes (h^+), hydroxyl radicals ($^{\bullet}OH$), and superoxide radical anions ($O_2^{\bullet-}$) species in the photocatalytic phenolic compound degradation, respectively.[30] The trapping experiment is similar to that of the photocatalytic degradation of phenolic compounds. The scavengers are added to the phenolic compounds solutions prior to the photocatalyst.

DOI: 10.1021/acsami.7b09026
ACS Appl. Mater. Interfaces 2017, 9, 35757–35774

2.8. Photoelectrochemical Measurements. Electrochemical measurements were conducted using a three-electrode electrochemical cell consisting of a platinum wire as the counter electrode, Ag/AgCl electrode as reference electrode, and a prepared electrode as the working electrode filled with an aqueous solution of 0.1 M Na_2SO_4. The electrolyte was saturated with nitrogen gas prior to electrochemical measurements. The photoelectrochemical measurements were performed using an Ivum multichannel potentiostat under illumination conditions (λ = 400 nm). Irradiation was performed using a 300 W Xe lamp with a 400 nm cutoff filter.

3. RESULTS AND DISCUSSION

3.1. Porosity of the Nanofibers. N_2 sorption isotherms and the pore diameter distributions of all the NFs are shown in Figure 1a, and a summary of the specific surface area, pore volume, and average pore diameter data is shown in Table S1 in Supporting Information. All the NFs are of typical *IV* isotherms with type H3 hysteresis loop according to the Brunauer–Deming–Deming–Teller (BDDT) classification, suggesting the presence of mesoporous structure.[31] The most important thing is that the materials showed intraparticle mesoporosity or "framework porosity".[32] This is because the hysteresis loops of Co_3O_4 NFs, CuO NFs, and composite Co_3O_4–CuO NFs start within a relative pressure (P/P_0) region of 0.1–0.5.[33] The formation of mesoporous structure within NFs is due to the removal of mixed PVP and PEG polymeric matrix at optimum calcinations temperature (450 °C in 4 h). The pore size distribution curve of all NFs is shown in the Figure 1a (inset). The intense peak of all NFs is at 2–50 nm, the resulting mesoporous range. The BET specific surface area, pore

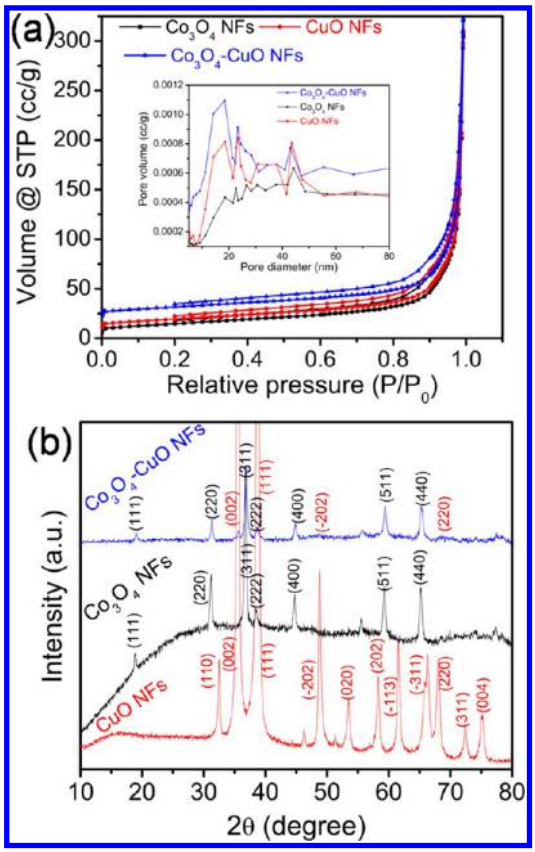

Figure 1. (a) N_2 sorption isotherm and pore diameter (inset) and (b) wide-angle X-ray diffractograms of mesoporous Co_3O_4, CuO, and composite Co_3O_4–CuO NFs.

diameter, and pore volume of the NFs are listed in Table S1. The specific surface areas of Co_3O_4 NFs, CuO NFs, and composite Co_3O_4–CuO NFs are 28, 35, and 39 m^2/g, respectively. The high surface area of NFs will provide more reactive sites for an interaction with phenolic compounds. The pore diameter (Table S1) are in the range of the mesoporous. Hence from the BET isotherm and pore diameter data, it is concluded that all NFs have mesoporous character within framework.

The wide angle XRD patterns of mesoporous Co_3O_4 NFs, CuO NFs, and composite Co_3O_4–CuO NFs are shown in the Figure 1b. In the XRD pattern of porous Co_3O_4 NFs, the Bragg reflections at angles of 18.86°, 31.16°, 36.92°, 38.56°, 44.67°, 59.28°, and 65.26° correspond to (111) (220), (311), (222), (400), (511), and (440) main crystal planes indicating the formation of pure cubic crystalline Co_3O_4 (JCDPS, card no. 42-1467). In the XRD pattern of mesoporous CuO NFs, the peaks at angles of 32.49°, 35.59°, 38.80°, 48.87°, 53.52°, 58.39°, 61.49°, 66.25°, 68.14°, 72.46°, and 75.23° were purely assigned to the (110), (002), (111), (−202), (020), (202), (−113), (−311), (220), (311), and (004) crystal planes, respectively. It can be seen that all the diffraction peaks belong to the CuO monoclinic phase (JCPDS 48-1548). The porous composite Co_3O_4–CuO NFs consisting of reflection planes (111), (220), (400), (222) (511), and (440) are due to cubic crystalline Co_3O_4, and crystal planes (002), (111), (−202), and (220) are due to monoclinic CuO. Hence, the presence of both Co_3O_4 and CuO reflection planes in mesoporous composite Co_3O_4–CuO NFs indicates the formation of Co_3O_4–CuO composite.

3.2. Morphological Analyses of Mesoporous Nanofibers. The morphologies of the mesoporous nanofibers were investigated by SEM images. Figure 2 describes the morphology, and Table S1 depicts the diameter of different mesoporous NFs before and after calcination. The PVP/PEG is used as mixed polymeric carrier matrix for the electrospinning of nanofibers. The nanofibrous materials before calcinations (dried 70 °C for 6 h) are denoted as, for example, PVP/Co_3O_4/PEG, whereas after calcination (removal of PVP and PEG at 450 °C, 4 h) they are denoted as mesoporous Co_3O_4 NFs. Similarly, the other NFs can be symbolized in order to describe the SEM morphology. The average diameter of mesoporous NFs is mentioned for all samples. The bead-free nanofibers with fiber diameter of 280 ± 50 nm for PVP/Co_3O_4/PEG NFs are obtained before calcination (Figure 2a). The rough and mesoporous nanofibers with narrow fiber diameter of 160 ± 30 nm for mesoporous Co_3O_4 NFs are obtained (Figure 2b) after calcinations of PVP/Co_3O_4/PEG. Similarly, bead-free and smooth fibrous morphology having diameter of 400 ± 40 nm is also observed for the sample of PVP/CuO/PEG in Figure 2c, whereas a rough, mesoporous nature and narrow diameter (130 ± 20 nm) for CuO NFs are obtained after calcination as depicted in Figure 2d. A clear mesoporous nature of CuO NFs framework is observed which is consistent with BET result. Moreover, Figure 2e shows the bead-free PVP/Co_3O_4–CuO/PEG NFs having diameter of 600 ± 70 nm with irregular and inhomogeneous structure having rectangular moieties which is marked in arrows. These rectangular moieties disappeared, and creation of mesoporosity appeared within blank space of rectangular voids (Figure 2f) as well as the diameter reduction of the NFs (250 ± 30 nm) which is due to the combined effect and removal of PVP and PEG in the optimum calcinations temperature, which resulted in mesoporous Co_3O_4–CuO NFs. Furthermore, in order to examine the role of PEG for

DOI: 10.1021/acsami.7b09026
ACS Appl. Mater. Interfaces 2017, 9, 35757–35774

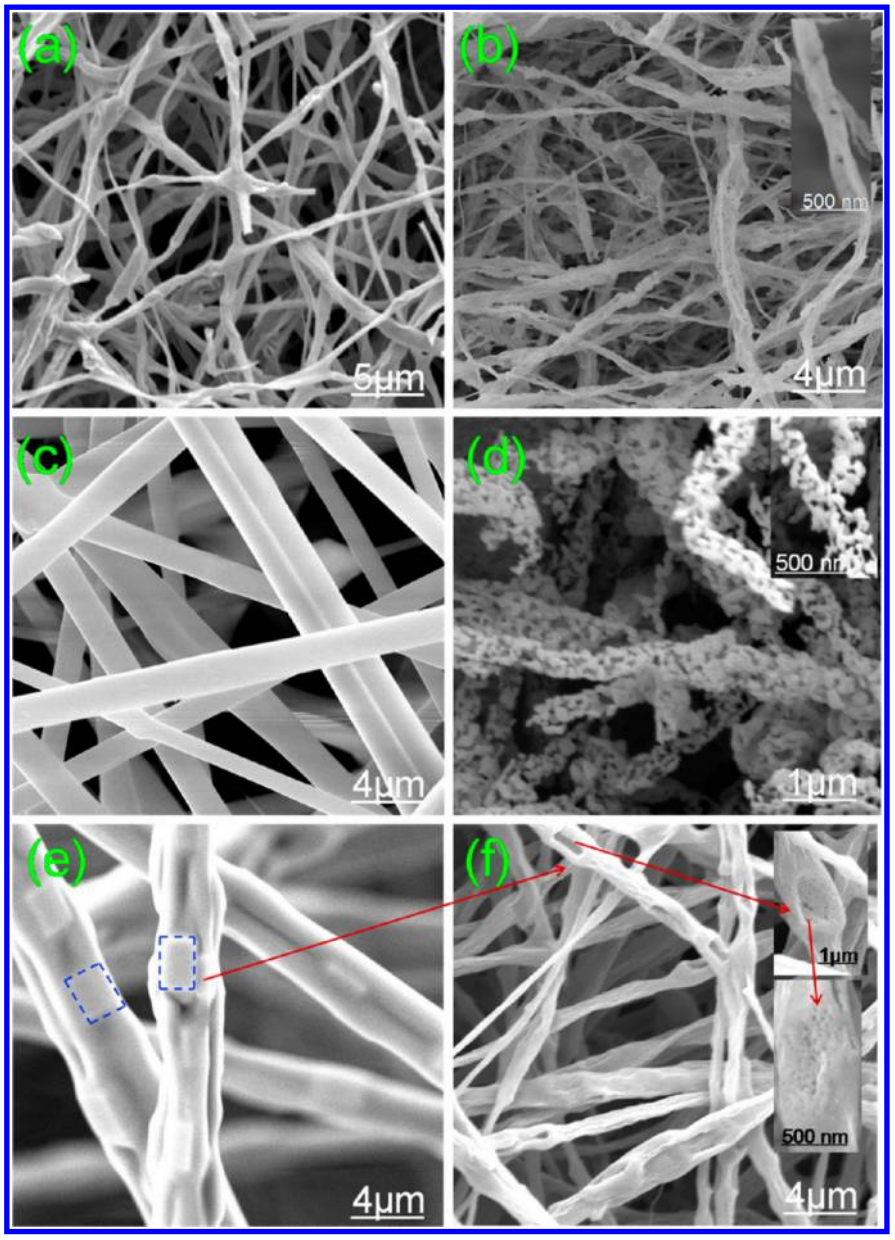

Figure 2. Representative SEM images of (a) PVP/Co_3O_4/PEG, (b) mesoporous Co_3O_4 NFs, (c) PVP/CuO/PEG, (d) mesoporous CuO NFs, (e) PVP/Co_3O_4–CuO/PEG, and (f) mesoporous Co_3O_4–CuO NFs.

generating mesoporosity, SEM image of porous CuO nanoflower is incorporated in the Supporting Information (Figure S1). The CuO nanoflowers enriched with porous morphology have been obtained from the neat PEG matrix. From Scheme 1, Figure 2, and Figure S1, it is understood that PEG is responsible for generation of porosity whereas PVP aids to create NFs and mixed PVP/PEG produces mesoporous NFs. The decrease of fiber diameter for all NFs and creation of mesoporosity after calcination is due to the removal/decomposition of PVP matrix and quick decomposition of PEG, respectively. In short, a combination of high molecular weight polymeric matrix (i.e., PVP) helps the electrospinning of the nanofibers, and low molecular weight polymeric template (i.e., PEG) helps to create mesoporosity once the NFs are calcined in order to obtain inorganic NFs by removal of polymeric components.

The TEM and HR-TEM analyses of the mesporous NFs have been performed in order to study the morphology and formation of nanoparticles (NPs) within NFs (Figure 3). Parts a and b of Figure 3 describe the TEM images of the mesoporous Co_3O_4 NFs. The highly porous nature is clearly observed, i.e., mesoporous within the Co_3O_4 NFs which was consistent with the BET analyses. The vital aspect of the present study is that Co_3O_4 NPs are interconnected in such a way that also aids formation of an empty void (mesoporosity). The particle size of the Co_3O_4 NPs is 16.5 ± 4 nm (Table S1). The formation of the mesoporus and NPs within NFs can have an architecture as "mesoporous–NPs–Co_3O_4 NFs". The similar micrographs were observed in the case of the mesoporous CuO NFs (Figure 3c,d) and also followed the similar architecture, i.e., "mesoporous–NPs–CuO NFs". The size of the interconnected CuO NPs is 20.0 ± 2.0 within CuO NFs. Hence, mesoporosity and interconnected NPs within both mesoporous CO_3O_4 and CuO NFs will enhance the surface reactive site and visible light absorption property through quantum confinement phenomena, respectively. These phe-

DOI: 10.1021/acsami.7b09026
ACS Appl. Mater. Interfaces 2017, 9, 35757–35774

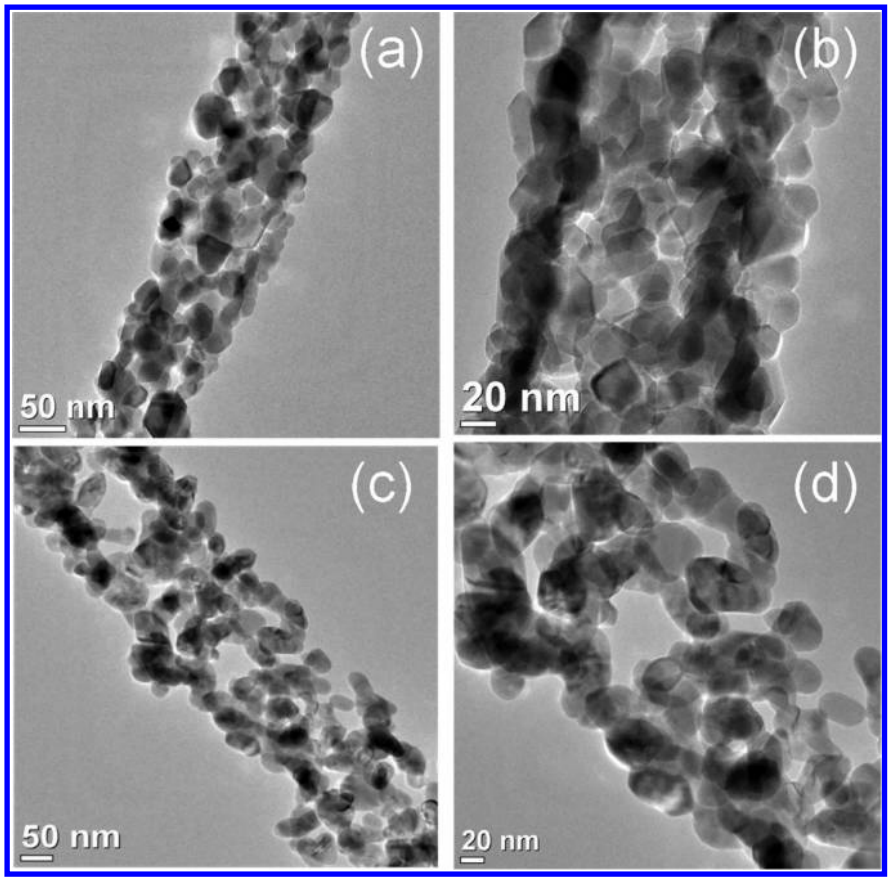

Figure 3. Representative TEM micrographs of mesoporous Co_3O_4 NFs (a, b) and mesoporous CuO NFs (c, d).

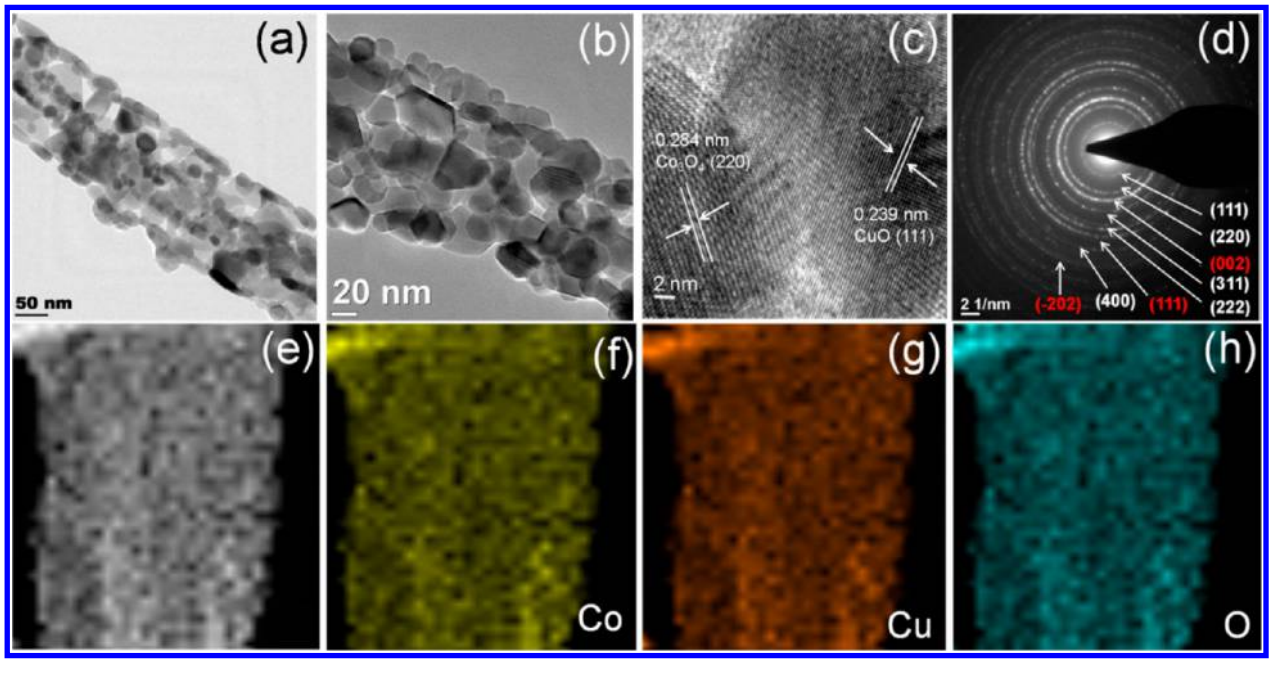

Figure 4. Representative micrographs of mesoporous composite Co_3O_4–CuO NFs: (a, b) TEM images; (c) HR-TEM image (lattice fringes); (d) SAED pattern; (e–h) EDAX mapping patterns.

nomena will be helpful for an efficient photocatalytic degradation of phenolic compounds in the visible light. The lattice fringes from HR-TEM and selected area electron diffraction (SAED) pattern of the Co_3O_4 NFs are displayed in the Figure S2a,b. The lattice spacing 0.286 nm is due the presence of Co_3O_4 with the plane (220) within the mesoporous Co_3O_4 NFs.[34] The SAED pattern exhibits the diffraction rings (111), (220), (311), and (222) of a spinel structure of Co_3O_4 in mesoporous Co_3O_4 NFs. The inset image in Figure S2b shows the fast Fourier transform (FFT) diffractogram from the

DOI: 10.1021/acsami.7b09026
ACS Appl. Mater. Interfaces 2017, 9, 35757–35774

mesoporous Co_3O_4 NFs with {110} direction.[21] The exposed surface active facets {110} are more reactive in the mesoporous Co_3O_4 NFs, which could absorb visible light efficiently. Figure S2c shows the HR-TEM image along with lattice spacing, and Figure S2d shows the SAED pattern of mesoporous CuO NFs. The lattice spacing 0.240 nm for (111) plane is due to the CuO monoclinic phase.[35] The SAED pattern exhibits the diffraction rings (110), (002), and (111), corresponding to the presence of CuO in the mesoporous CuO NFs. The facets {001} are observed from FFT diffractogram Figure S2d (inset), which is the highly active facets of the CuO.[28] The reactive facets {110} from Co_3O_4 and {001} from CuO will enhance the photocatalytic properties through light absorption phenomena.

The TEM and HR-TEM images of the mesoporous composite Co_3O_4–CuO NFs are shown in Figure 4, and particle size within NFs is listed in the Table S1. Figure 4a,b shows that the porous nature, i.e., mesoporous, is confirmed from BET analyses. The TEM imaging (Figure 4a,b) also indicated that the enriched Co_3O_4 and CuO NPs are interconnected with each other within composite Co_3O_4–CuO NFs. The particle size of NPs within composite Co_3O_4–CuO NFs is measured as 15.2 ± 3.0 nm (Table S1). Hence, the architecture of "mesoporous–NPs–Co_3O_4–CuO NFs" is formed which is similar to those of the other two NFs (Co_3O_4 NFs and CuO NFs). From the HR-TEM imaging (Figure 4c), the lattice spacing of 0.284 nm for Co_3O_4 (220) and 0.239 nm for CuO (111) was measured within the mesoporous composite Co_3O_4–CuO NFs.[34,35] The decrease of the lattice spacing in Co_3O_4 and CuO within composite as compared to the neat Co_3O_4 and CuO NFs is due to the formation of the composite Co_3O_4–CuO NFs. The lattice fringes showing the polycrystalline nature are due to the presence of Co_3O_4 and CuO. The SAED pattern (Figure 4d) exhibits the diffraction rings (111), (220), (311), (222), and (400) corresponding to the crystalline nature of the spinel structure of Co_3O_4, and the plane corresponding to (002), (111), and (−202) is due to the monoclinic structure of CuO (marked in red) within mesoporous composite Co_3O_4–CuO NFs. The polycrystalinity nature of mesoporous Co_3O_4–CuO NFs is also helpful for enhancement of the light absorption property. In order to confirm the distribution of elements and reactive sites on the surface of mesoporous composite Co_3O_4–CuO NFs, EDAX elemental mapping analysis is employed (Figure 4e–h). The EDAX mapping results revealed the high content of Co as compared to Cu in Co_3O_4–CuO NFs, which is consistent with the experimental condition. The EDAX elemental analyses of mesoporous Co_3O_4 NFs, CuO NFs, and composite Co_3O_4–CuO NFs reveal the presence of respective elements in each sample of NFs (Figure S3).

3.3. Optical Analyses of Mesoporous Nanofibers. The optical properties such as absorption edges, effect of composite on the electronic structure, and band gap energy of the mesoporous Co_3O_4 NFs, CuO NFs, and composite Co_3O_4–CuO NFs are studied by using UV–visible absorption spectra (Figure 5a). The entire mesoporous NFs showed strong absorption band at 200–300 nm, which is due to the ligand to metal charge transfer (LMCT) between oxygen and metal center within the NFs. The mesoporous CuO NFs exhibit continuous and enhanced light absorption in the range of 400–800 nm. This is due to the efficient harvesting of visible light. Moreover, the octahedrally coordinated Cu^{2+} species is observed at 600–800 nm which is due to the d–d transition band.[36] A broad peak starting from 400–670 nm is due to the

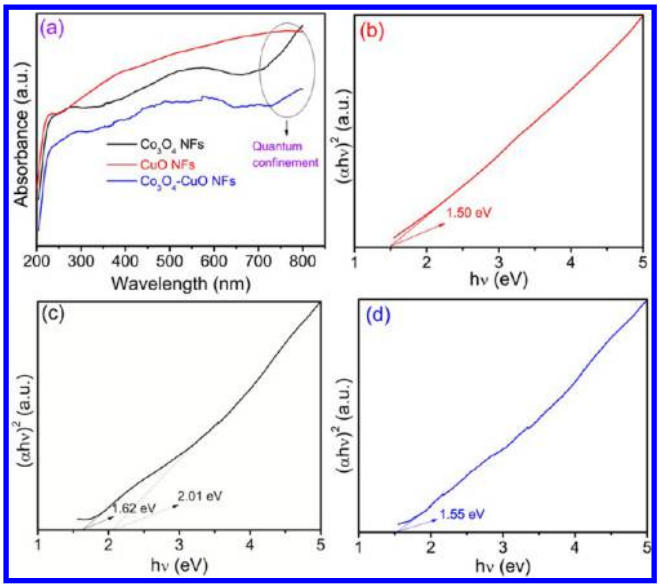

Figure 5. (a) UV–visible absorption spectra of mesoporous NFs samples, showing plots of $(\alpha h\nu)^2$ vs photon energy $(h\nu)$ for the band gap energy of (b) mesoporous CuO NFs, (c) mesoporous Co_3O_4 NFs, and (d) mesoporous composite Co_3O_4–CuO NFs.

d–d transitions of Co^{3+} in octahedral sites and Co^{2+} in tetrahedral sites in mesoporous Co_3O_4 NFs.[37] The d–d transition of octahedral and tetrahedral sites helps light absorption in the visible region. The mesoporous composite Co_3O_4–CuO NFs shows the dual behavior of d–d transitions of Co^{3+} and Co^{2+} along with Cu^{2+} charge transfer in the peak region 400–712 nm. The dominant nature Co_3O_4 absorption peak in composite Co_3O_4–CuO NFs is due to the composition of high amount of Co_3O_4 with less amount of CuO. The most interesting finding of the present investigation is the rising or red shifting of peaks from 720 to 800 nm in all mesoporous NFs. This phenomenon may be due to the creation of quantum confinement phenomena in mesoporous Co_3O_4 NFs, CuO NFs, and composite Co_3O_4–CuO NFs. All presently fabricated NFs showing red shifts which favor high photocatalytic applications in the visible region. The band gap energy of all NFs materials can be calculated by using the following equation.[38]

$$\alpha h\nu = A(h\nu - E_g)^n$$

where α, ν, A, and E_g are the absorption coefficient, light frequency, proportionality constant, and band gap, respectively. The band transition depends upon the value of $n = {}^1/_2$ for direct transition and $n = 2$ for indirect transition. It is examined that all the mesoporous NFs show direct allowed transitions. The band gap energies of the all NFs can be estimated from the plots of $(\alpha h\nu)^2$ versus photon energy $(h\nu)$. The intercept of the tangent to the X axis would give a good approximation of the band gap energies for the NFs samples, as shown in Figure 5b,c,d. The band gap of mesoporous CuO NFs (Figure 5b) is found to be 1.50 eV, which belongs to the visible light response semiconductor. The observed band gap value is wider than the bulk CuO (1.2 eV), which is due to the quantum confinement effect for mesoporous CuO NFs. The wider band gap of mesoporous CuO NFs as compared to bulk is due to efficient light absorption by mesoporous NPs and crystalline CuO NFs, confirmed from TEM and HR-TEM analyses. It is well-understood that the reduction in particle size results in

DOI: 10.1021/acsami.7b09026
ACS Appl. Mater. Interfaces 2017, 9, 35757–35774

increased surface/volume ratio.[39] The increase of band gap energy in NFs as compared to bulk material is due to the lowering of the coordination number and atomic interaction of surface atom which leads to increases of the highest valence band energy and decreases of the lowest unoccupied conduction band energy.[40] The mesoporous Co_3O_4 NFs (Figure 5c) has two E_g with values of 1.62 (E_{g1}) and 2.01 eV (E_{g2}), which agreed with the band structure of Co_3O_4 with Co^{3+} $t_{2g} \rightarrow Co^{2+}$ t_{2g} (E_{g1}) and $O^{2-} \rightarrow Co^{2+}$ t_{2g} (E_{g2}) charge-transfer transition, respectively.[41] It is evaluated that the band gap values for bulk Co_3O_4 are 1.48 eV (E_{g1}) and 2.19 eV (E_{g2}).[13] The E_{g1} value Co_3O_4 NFs is 1.62 eV which is wider than the E_{g1} value of bulk Co_3O_4 (1.48 eV). This is due to the quantum confinement effect and lattice contraction. Furthermore, the E_{g2} value of Co_3O_4 NFs is 2.01 eV which is smaller than the E_{g2} value of bulk Co_3O_4 (2.19 eV). This can be attributed to several factors such as lattice expansion and/or the presence of defects (mainly vacancies) in the intergranular regions which forms the donor and acceptor bands.[42] The mesoporous composite Co_3O_4–CuO NFs (Figure 5d) has band gap of 1.55 eV. The narrow band gap as compared to Co_3O_4 NFs is due to the formation of localized state by intermixing of Co 2p and Cu 2p. The most interesting finding is that the band gap of Co_3O_4–CuO NFs is wider than the bulk CuO and Co_3O_4, which proves the availability of quantum confinement effect and defect/vacancies sites. Hence, the optical properties of the fabricated mesoporous NFs have quantum confinement, defect/vacancies, and suitable band gap which could enhance the light absorption property in the visible region for an efficient photocatalytic degradation of organic pollutants.

In order to prove the quantum confinement phenomena more clearly within mesoporous NFs, the UV–vis–NRI DRS studies have been performed and the obtained spectra were given in the Supporting Information (Figure S4). In the UV–visible absorption spectra (Figure 5a), the optical behavior of the mesoporous NFs from 200 to 720 nm is already discussed. Hence, in the UV–vis–NRI DRS, the discussion regarding optical properties of the fabricated NFs was focused from 720 to 2000 nm. The interesting and rare finding observed is that all mesoporous NFs have the quantum confinement effect. The high red shifting peaks starting from nearly 780 to 1000 nm is due to the quantum confinement effect for all NFs. The d–d transition band for tetrahedrally coordinated Cu^{2+} species appears around 1300–1600 nm for CuO NFs.[43] In both Co_3O_4 NFs and Co_3O_4–CuO NFs, the shoulder peak starting from 1020–1210 nm is due to the "intervalence" charge-transfer $Co^{2+} \rightarrow Co^{3+}$ and the peak at 1700 nm is attributed to the $^4A_2(F) \rightarrow {}^4T_1(F)$ transition in the Co_3O_4 structure. The charge transfer transition represents an internal oxidation–reduction process which facilitates photocatalytic process in the visible region. Hence, from UV–visible absorption and UV–vis–NRI DRS spectra it is concluded that high red shifting of all mesoporous NFs is due to the quantum confinement effect and the internal charge transfer within Co^{2+} and Co^{3+} and Cu^{2+}.

The photoluminescence (PL) emission spectra describe the effectiveness of the charge carrier trapping, immigration, and transfer behaviors of the photoexcited electron–hole pairs in semiconductors. The PL emission (λ_{exc} = 390 nm) spectra of semiconductor mesoporous Co_3O_4 NFs, CuO NFs, and composite Co_3O_4–CuO NFs are shown in Figure 6. For all mesoporous NFs the peaks centered at 442, 470, and 550 nm correspond to the blue, green, and yellow-orange bands, respectively. The blue-shift behavior of the intense peak

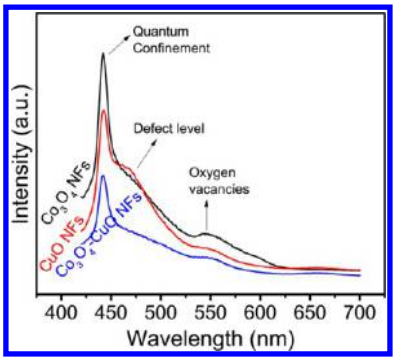

Figure 6. Photoluminescence spectra of mesoporous Co_3O_4, CuO, and composite Co_3O_4–CuO NFs.

position at 442 nm for all NFs is due to the Burstein–Moss effect resulting from nanostructure materials, which is provided with the enhanced quantum confinement effect.[44] The intense peak for all NFs at blue region is due to the electron excitation, and the weak green emission (470 nm) is due to the deep level defect.[45] Moreover, the yellow-orange shift (550 nm) is due to the oxygen vacancies (V_o). For mesoporous Co_3O_4 NFs, the emission peaks 442, 470, and 550 nm correspond to charge transfer $O^{2-} \rightarrow Co^{2+}$ process, $O^{2-} \rightarrow Co^{3+}$ charge transfer, and oxygen vacancies (V_o), respectively.[46] Likewise, mesoporous CuO NFs exhibit the copper vacancy (V_{Cu}), Cu interstitial (I_{Cu}), oxygen vacancy (V_o) corresponding to the emission peaks at 442, 470, and 550 nm, respectively.[47] The mesoporous composite Co_3O_4–CuO NFs also show the blue and yellow-orange emission peaks, resulting quantum confinement effect, and oxygen vacancies. From the above investigation, it is well-understood that the all mesoporous NFs exhibit quantum confinement effect (blue region), crystal defect (green region), and oxygen vacancies (yellow-orange region). Quantum confined effect provides high light absorption property of nanofibers due presence of NPs within all NFs, which provides high surface to volume ratio. According to the Marcus theory, quantum confined effect favors higher rates of interfacial charge transfer due to the increased thermodynamic energy of the confined electron–hole pairs.[48] Hence, formation of interfacial charge transfers in all NFs increases the generation of electron–hole for photocatalytic application in visible region. The defect level indicates the radiative recombination resulted in increase in the PL intensity.[49] The green emission peak (470 nm) completely vanished in the case of mesoporous composite Co_3O_4–CuO NFs as compared to Co_3O_4 and CuO NFs, indicating the prevention of electron–hole recombination. This phenomenon proves the role of CuO as cocatalyst in Co_3O_4. Moreover, the oxygen vacancies of all NFs are situated at 550 nm. Oxygen vacancies aid to trap the photoemission electron from conduction band of fabricated NFs via nonradiative transition. This phenomenon prevents the electron–hole recombination and resulting swift photocatalytic degradation of phenolic compounds in visible light. Furthermore, the Schottky barrier appears to be due to the mixing of the CuO into the Co_3O_4. This phenomenon also helps to create superficial space charge layer between valence and conduction band of Co_3O_4 NFs, which could act as an electron sink to efficiently prevent the electron–hole recombination.[50] That is why PL intensity gradually decreases from Co_3O_4NFs > CuO NFs > Co_3O_4–CuO NFs.

3.4. Chemical Structure Analyses of Nanofibers. X-ray photoelectron spectroscopy (XPS) analysis has been performed

DOI: 10.1021/acsami.7b09026
ACS Appl. Mater. Interfaces 2017, 9, 35757–35774

to investigate the electronic environment and oxidation state of mesoporous composite Co_3O_4–CuO NFs (Figure 7). It has

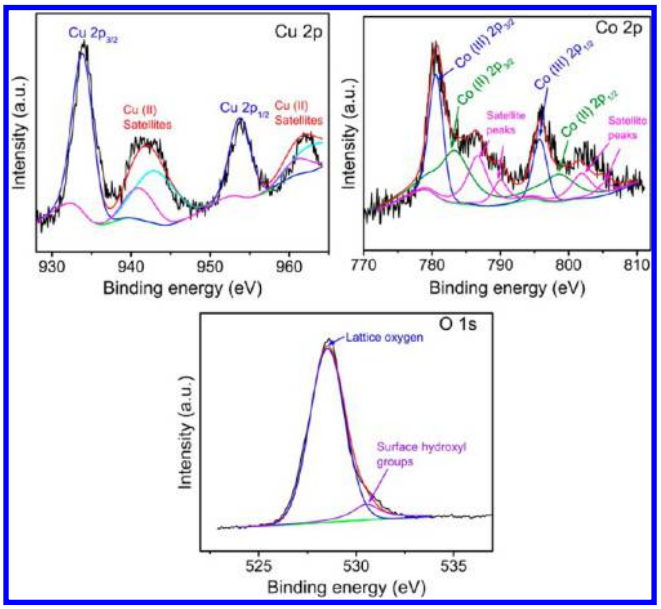

Figure 7. Cu 2p core level spectrum, Co 2p spectrum, and O 1s spectrum in the mesoporous composite Co_3O_4–CuO NFs.

been investigated that the main peaks are at ~933.4 eV (Cu $2p_{3/2}$) and 953.2 eV (Cu $2p_{1/2}$), along with the presence of their characteristic shakeup satellite peaks at approximately 941.3 and 961.5 eV, respectively, which are due to the existence of pure CuO.[51] In the present study, the binding energy (BE) of Cu $2p_{3/2}$ and Cu $2p_{1/2}$ is at approximately 933.77 and 953.71 eV, indicating fully oxidized CuO [52] in mesoporous composite Co_3O_4–CuO NFs. The shakeup satellite peaks located at approximately 940.75, 942.80, and 961.37, 962.41 eV are attributed to the Cu (3d) hole states.[53] These satellite peaks also confirm the Cu(II) bonding state of CuO in the composite Co_3O_4–CuO NFs.[54] The XPS spectrum of Co 2p in Figure 7 shows that the peaks at approximately 780.52, and 795.70 eV correspond to Co(III) $2p_{3/2}$ and $2p_{1/2}$, while 783.4 and 798.6 eV correspond to Co(II) $2p_{3/2}$ and $2p_{1/2}$, respectively. The weak $2p_{3/2}$ satellite peaks are found at approximately 786.6 and 790.01 eV, and those of $2p_{1/2}$ satellite peaks are found at approximately 802.00 and 805.30 eV.[55] These peaks represent the existence of Co(II) in the tetrahedral sites and Co(III) in the octahedral sites of Co_3O_4 in the mesoporous composite Co_3O_4–CuO NFs. The observed energy separation between Co(III) $2p_{3/2}$ and Co(III) $2p_{1/2}$ peaks is 15 ± 0.2 eV, corresponding to the Co_3O_4. The O 1s BE in composite Co_3O_4–CuO NFs is observed at ~528.54 eV and is due to the strong interaction of O with Co and Cu in mesoporous composite Co_3O_4–CuO NFs, whereas peak at ~530.63 eV (lattice oxygen) is due to the surface hydroxyl present in the mesoporous composite Co_3O_4–CuO NFs.[56] From the above results it is concluded that the higher of BE of Co 2p as compared to pure Co 2p (Rakibuddin et al.)[57] and lower BE of 528.54 eV as compared to 529 eV pure Co_3O_4 [57] are due to the electron transfer from Co(II)/Co(III) to Cu(II) through O atom and forming the −Co−O−Cu− linkage in the mesoporous composite Co_3O_4–CuO NFs.

The FTIR spectra of Co_3O_4NFs, CuO NFs, and Co_3O_4–CuO NFs are displayed in the Figure S5. The FTIR spectrum of the mesoporous Co_3O_4 NFs exhibits two distinct bands at 567 and 663 cm^{-1} and are due to the stretching vibrations of the metal−oxygen bonds.[58] The first band at 567 cm^{-1} is assigned to the OB_3 vibration, where B denotes Co^{3+} in the octahedral hole. The band at 663 cm^{-1} is assigned to the ABO_3 vibration, where A denotes Co^{2+} in the tetrahedral hole. Hence, nature of the mesoporous Co_3O_4 NFs is spinel lattice. The Cu−O stretching vibration observed at 535 cm^{-1} is due to the formation of CuO in mesoporous CuO NFs.[59] The stretching frequencies 553 and 661 $cm^{-1}$are due to the presence of Co^{3+}/Cu^{2+} and Co^{2+} in the mesoporous composite Co_3O_4–CuO NFs, respectively. That means the formation of spinel Co_3O_4 and CuO is observed within composite Co_3O_4–CuO NFs.

The SERS experiment was performed by incident of laser (532 nm) to the bare mesoporous Co_3O_4 NFs, CuO NFs, and composite Co_3O_4–CuO NFs in comparison with addition of probe molecule rhodamine 6G (Rh 6G) mixed with mesoporous NFs separately (Figure S6). From Figure S6, it is investigated that all the mesoporous NFs mixed with Rh 6G have high enhancement of Raman intensity as compared to neat mesoporous NFs. The enhancement of Raman intensity is due to the presence of NPs within the mesoporous NFs. The NPs present in all the mesoporous NFs efficiently adsorb Rh 6G because of the quantum confinement phenomena, which leads to the absorption of the laser radiation and enhancement of the Raman intensity of Rh 6G. This enhancement of Raman intensity in the presence of NPs within mesoporous NF is called as SERS enhancement. The SERS signals due to the addition of Rh 6G are 1646 cm^{-1}, 1567 cm^{-1}, 1495 cm^{-1}, 1362 cm^{-1}, 1309 cm^{-1}, and 1184 cm^{-1}. These Raman signals arose from the totally symmetric modes of in-plane C−C stretching vibrations of Rh 6G.[60] The Raman band at 772 cm^{-1} was assigned to the C−H out-of plane bending vibration of Rh 6G. The shift at 608 cm^{-1} was assigned to the in-plane bending vibration of the Rh 6G C−C−C ring.[61] The SERS enhancement is based on the two types of mechanisms: the first is the electromagnetic enhancement, which is caused by a strong surface plasmon resonance of the nanoparticles metal surface coupled to the incident light.[62] The second is the chemical enhancement, which can be considered to be a resonance Raman process between the ground electronic state of the molecule−metal complex and its new excited levels arising from charge transfer between the metallic surface and the adsorbed molecule.[63] It should be noted that semiconductor materials have dominant contribution for the SERS signal, which must involve a charge-transfer mechanism since surface plasmon resonances lie far in the infrared.[63] In the present context, interconnected NPs situated in the mesoporous Co_3O_4 NFs, CuO NFs, and composite Co_3O_4–CuO NFs belong to semiconductor, interacting with molecule (Rh 6G) through charge transfer mechanism. It has been noted that the quantum confinement phenomenon arises in the small size of the semiconductor NPs. The surface resonance happens only in the small size NPs which leads to excite the laser energy. Hence, the NPs size of the mesoporous Co_3O_4 NFs, CuO NFs, and composite Co_3O_4–CuO NFs is 16.5 ± 4, 20.0 ± 2, and 15.2 ± 3, respectively. The present interconnected NPs mediated mesoporous NFs have internal charge transfer phenomena and semiconductor behavior, proved from UV−vis absorption and UV−vis DRS spectra. These NPs adsorb Rh 6G molecule efficiently which provides the good platform for the excitation of the laser through charge transfer mechanism. The charge transfer process enhances the SERS signals. Conclusively,

DOI: 10.1021/acsami.7b09026
ACS Appl. Mater. Interfaces 2017, 9, 35757−35774

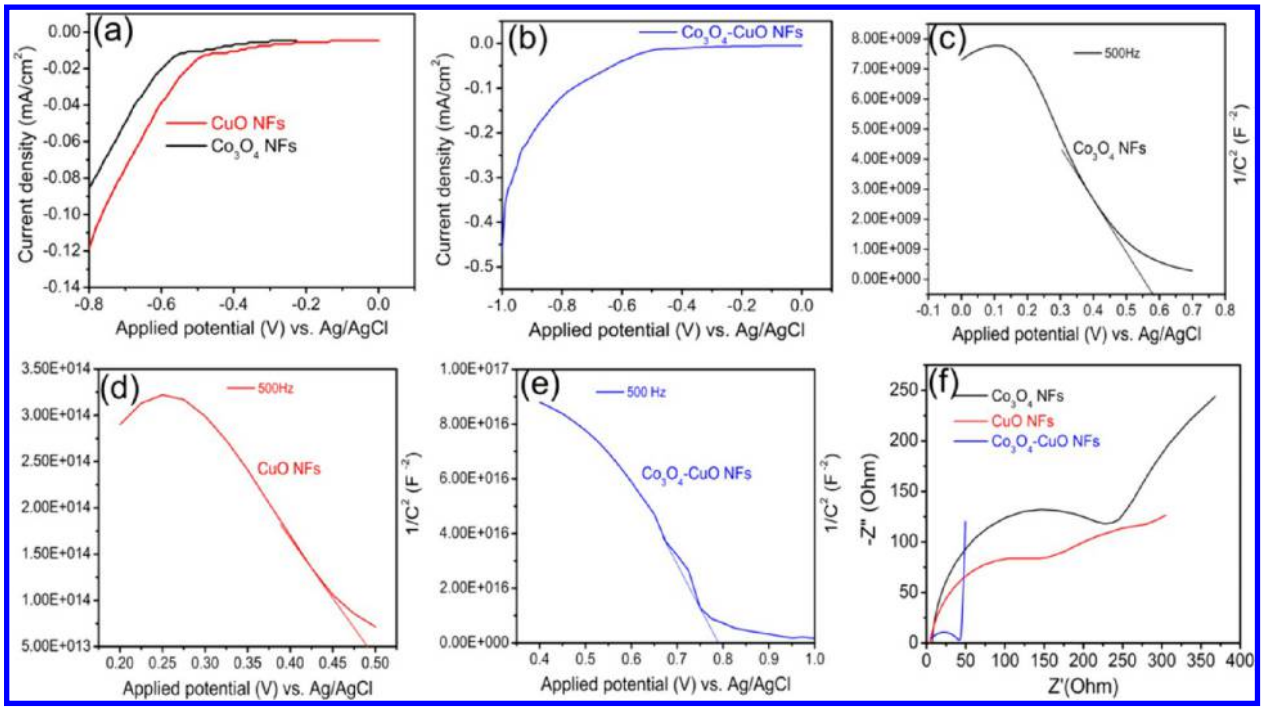

Figure 8. Potential−current density curves of mesoporous Co_3O_4 NFs, CuO NFs (a, b) and composite Co_3O_4−CuO NFs (c) under light condition. Mott−Schottky plots of mesoporous Co_3O_4 NFs, CuO NFs, and composite Co_3O_4−CuO NFs (c−e) under dark. Nyquist plot for the Co_3O_4 NFs, CuO NFs, and composite Co_3O_4−CuO NFs (f).

enhancement of SERS signals proves the quantum confinement effect of the interconnected NPs within all mesoporous NFs.

3.5. Electrochemical Studies of Nanofibers. In order to check the origin of the high photoactivity of the mesoporous composite Co_3O_4−CuO NFs along with neat mesoporous Co_3O_4 NFs and CuO NFs, photocurrent measurement, Mott−Schottky (MS) plots and electrochemical impedance spectroscopy (EIS) were employed to investigate the current generation, the majority carrier density, and charge transfer rate at the electrode/electrolyte interface inside mesoporous NFs. The photocurrent under light illumination of mesoporous Co_3O_4 NFs, CuO NFs, and composite Co_3O_4−CuO NFs was measured in 0.1 M Na_2SO_4 at a scan rate of 10 mV s^{-1} under light irradiation ($\lambda \geq 400$ nm). Parts a and b of Figure 8 shows the photocurrent densities of the mesoporous Co_3O_4 NFs, CuO NFs, and composite Co_3O_4−CuO NFs are measured to be −0.085 mA/cm^2, −0.012 mA/cm^2, and −0.44 mA/cm^2, respectively. The negative values of the photocurrent densities of all NFs represent the cathodic current and are due to the p-type nature of the semiconductor. The generation of the photocurrent in all NFs photocathodes is due to the mesoporosity and NPs within NFs morphology, whereas high generation of photocurrent density in Co_3O_4−CuO NFs photocathode as compared to other NFs is due to the charge transport phenomena.[64] The charge transport phenomena of Co_3O_4 could be improved by the CuO in composite Co_3O_4−CuO NFs. This charge transport phenomena prove the role of CuO as cocatalyst and enhancement of the photocatalytic performance.

The Mott−Schottky method helps to determine the band structure and recombination behavior, which are studied under dark conditions in three-electrode systems using Ag/AgCl as the reference electrode and platinum as the counter electrode dipped in 0.1 M Na_2SO_4 at pH 6.5 in 500 Hz.The Mott−Schottky plots of mesoporous Co_3O_4 NFs, CuO NFs, and composite Co_3O_4−CuO NFs are represented in Figure 8c−e.The observed negative slope for all three materials indicates that all are in p-type semiconductor. The single slope for the composite Co_3O_4−CuO NFs indicates that semiconductor Co_3O_4 is vitally involved in the photocatalytic performance with CuO as cocatalyst. Furthermore, from the intercept of the Mott−Schottky plots (Figure 8c−e), the flat band potentials (E_{fb}) for mesoporous Co_3O_4 NFs, CuO NFs, and composite Co_3O_4−CuO NFs are estimated to be 0.57, 0.48, and 0.78 V vs Ag/AgCl, respectively. As is well-known, a higher E_{fb} value for a p-type semiconductor implies a higher degree of band bending and a larger space-charge-region potential. Therefore, the high E_{fb} value of the composite Co_3O_4−CuO NFs provides a large driving force for the photoinduced electron−hole pairs to separate in the space charge region and then results in a high photoactivity toward phenolic compound degradation. The E_{fb} is approximately equal to the valence band potential for p-type semiconductors. Hence, the positions of the VB band for mesoporous Co_3O_4 NFs and CuO NFs are 0.57 and 0.48 V, respectively. This band structure has greatly contributed toward the photocatalytic activities which are discussed in the next section.

The electrochemical impedance spectroscopy (EIS) is studied in Figure 8f. The Nyquist plots of the mesoporous Co_3O_4 NFs, CuO NFs, and composite Co_3O_4−CuO NFs are showing semicircles at higher frequency level and almost a straight line inclined at a certain angle at lower frequency level. The semicircle at low frequencies features the charge transfer across the electrode/electrolyte interface, and the diameter of the semicircle represents the charge transfer resistance (R_{ct}).[65] The electron charge transfer resistance (R_{ct}) is estimated from the diameter of the semicircle. Here, the value of R_{ct} in different mesoporous NFs has the following trend: Co_3O_4 NFs (~225Ω) > CuO NFs (~156 Ω)> Co_3O_4−CuO NFs (~40.5Ω). It has been observed that the larger is the semicircle

DOI: 10.1021/acsami.7b09026
ACS Appl. Mater. Interfaces 2017, 9, 35757−35774

Scheme 2. Formation Mechanism of Mesoporous Composite Co_3O_4–CuO NFs in Both Chemical and Pictorial Approaches

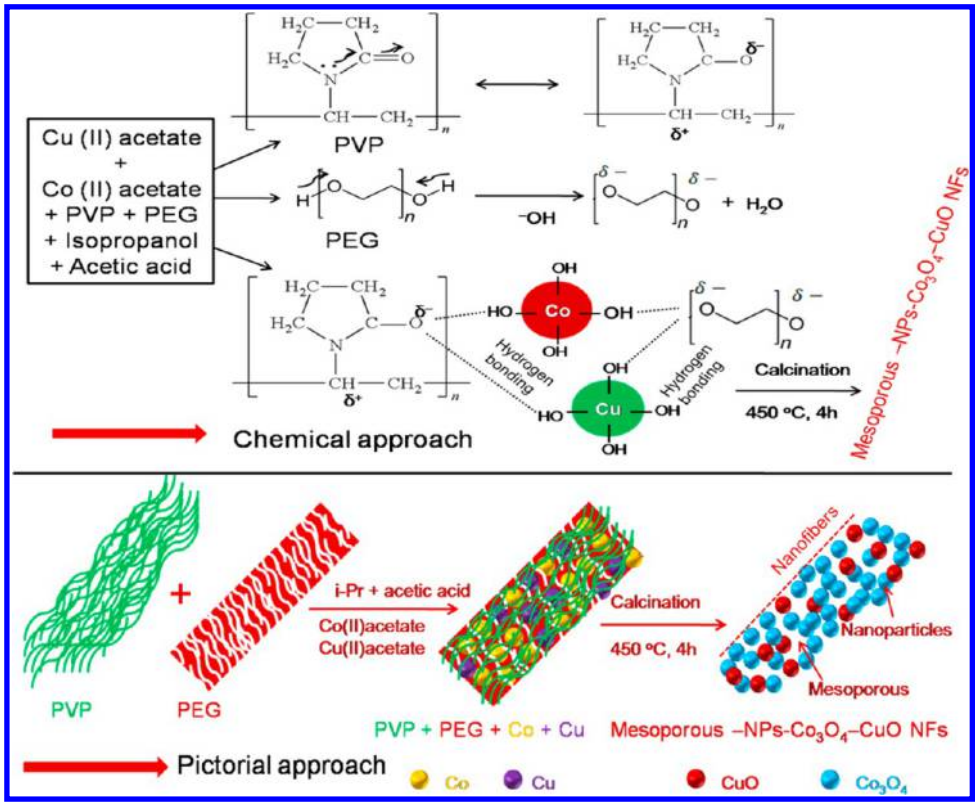

diameter, the greater is the resistance at the interface and the lesser is the conductance. The lower R_{ct} value shows that charge transfer is more efficient at the electrode/electrolyte interface with the incorporation of the cocatalysts, thus enhancing generation of photocurrent.[66] That means the lower R_{ct} value of mesoporous composite Co_3O_4–CuO NFs has high charge transfer ability. The charge transfer process could be efficiently progressed from Co_3O_4 to CuO, establishing the CuO as cocatalyst. Hence, the composite Co_3O_4–CuO NFs have high charge separation efficiency as compared to the constituent semiconductor NFs. Thus, the decreased value of R_{ct} increases the photocatalytic activity of the synthesized Co_3O_4–CuO NFs. Moreover, the straight line part in the lower frequency region is related to Warburg impedance (W_s), which results from the transfer or diffusion of ions in the electrolyte.[67] In Figure 8f, it is clearly visible that the Warburg region is small in the cases of the mesoporous composite Co_3O_4–CuO NFs and larger in Co_3O_4 NFs. The smaller Warburg region of the mesoporous composite Co_3O_4–CuO NFs as compared to single NFs indicates that the ion movement is more effective within the NFs through pores and favors the high photocatalytic performance of composite Co_3O_4–CuO NFs. Conclusively, the high current density, charge transfer, and ion movement in the composite Co_3O_4–CuO NFs due to the combination of CuO as cocatalyst and mesoporosity within NFs are responsible for the enhancement of photocatlytic performance.

3.6. Formation Mechanism of Mesoporous Composite Co_3O_4–CuO NFs. The possible formation mechanism of mesoporous composite Co_3O_4–CuO NFs is explained on the basis of the above experiments, which is illustrated in the Scheme 2. Scheme 2 depicts both the chemical approach and the pictorial approach. The chemical approach gives the idea about the chemical bonding interaction, whereas the pictorial approach tells about surface arrangements. The mesoporous composite Co_3O_4–CuO NFs are fabricated on the basis of in situ electrospinning method. PVP is a highly soluble polar polymer mixed with another polar polymer PEG in isopropanol. When precursors of Co and Cu are dissolved in the mixed polymer solution and acetic acid, then the hydrolyzed Co and Cu precursors, i.e., hydroxides of Co and Cu, make hydrogen bonds with partial anionic form of oxygen present in PVP and PEG. The slow hydrolysis of metal precursors leads to strong interaction with PVP and PEG matrix, resulting in PVP/Co_3O_4–CuO/PEG (dried at 70 °C for 5 h). The mesoporous composite Co_3O_4–CuO NFs, i.e., architecture of "mesoporous–NPs–Co_3O_4–CuO NFs", are formed after calcinations of PVP/Co_3O_4–CuO/PEG at 450 °C for 4 h. The role of PVP, PEG, and acetic acid has great importance for the fabrication of the mesoporous composite Co_3O_4–CuO NFs. PVP is responsible for providing the nanofibers framework during the electrospinning process because high molecular weight long chain PVP produces the long chain hydrogen bonding with hydroxyl group of Co and Cu. PEG is a polymer of hydrophilic chain. The hydrophilicity of the PEG chain is responsible for the more significant pore formation effect.[68] It has been reported that the additives that are generating foam during hydrolysis aids to form mesoporous nanofibers.[69] In the present study, after addition of PEG, foams are generated in the solution, leading to formation of mesoporosity in the composite Co_3O_4–CuO NFs. It has been noted that the PEG is used as the capping agent for the fabrication of the nanoparticles.[70] Hence, Co_3O_4 and CuO NPs are formed within mesoporous NFs by the role of PEG as capping agent through Ostwald ripening phenomena. The optimum concentration of the acetic acid helps to maintain the viscosity and solubilize the polymeric matrix. Conclusively,

DOI: 10.1021/acsami.7b09026
ACS Appl. Mater. Interfaces 2017, 9, 35757–35774

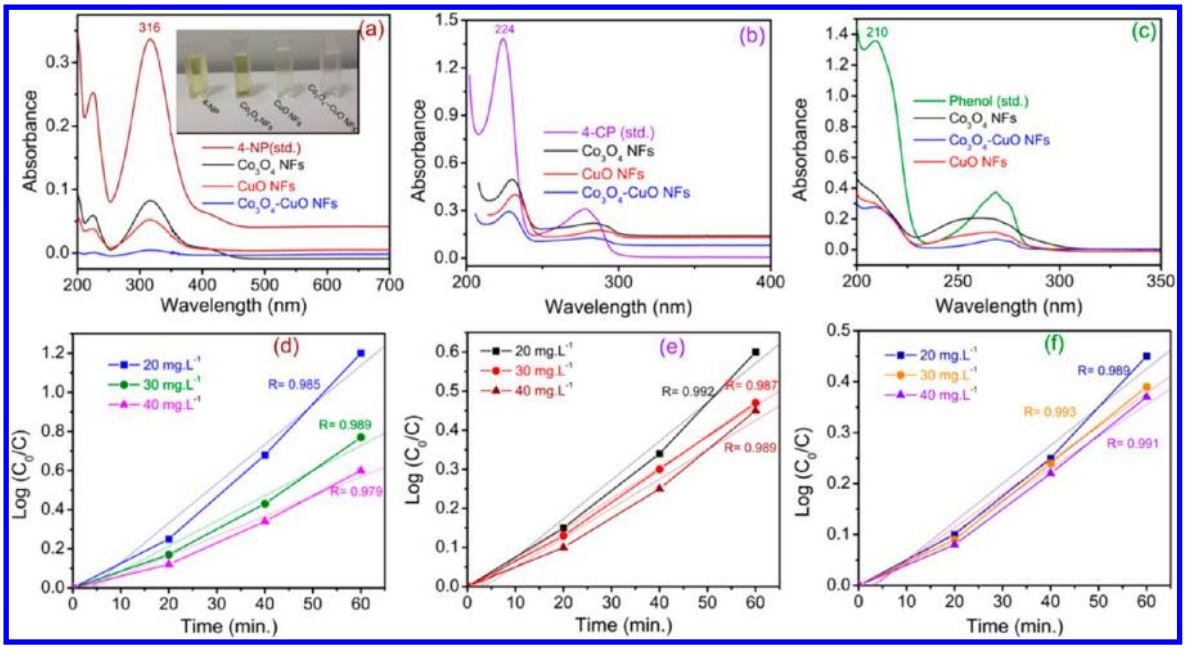

Figure 9. UV−vis spectra of the solutions recorded after photocatalytic degradation of phenolic compounds such as (a) 4-NP, (b) 4-CP, and (c) phenol by different photocatalysts. The degradation process is carried out by using different 10 mg of photocatalyst in a 10 mL phenolic compounds solution at pH 6 in visible light for 70 min. The kinetic study is also performed by taking different concentrations (20, 30, and 40 mg·L^{-1}) of phenolic compounds like (d) 4-NP, (e) 4-CP, and (f) phenol with different time intervals (20, 40, and 60 min) on mesoporous composite Co_3O_4−CuO NFs.

PVP, PEG, and acetic acid have great role in the fabrication of mesoporous composite Co_3O_4−CuO NFs or architecture of "mesoporous−NPs−Co_3O_4−CuO NFs".

3.7. Visible Light Photocatalytic Activity of Mesoporous Nanofibers. Photocatalytic degradation of phenolic compounds such as 4-nitrophenol (4-NP), 4-chlorophenol (4-CP), and phenol took place in the presence of visible light. It is observed that mesoporous composite Co_3O_4−CuO NFs (Co:Cu = 1/4) have high photocatalytic degradation activity toward phenolic compounds. The reaction was carried out for 70 min in the presence of visible light, 20 mg·L^{-1} of phenolic compounds, and 1 mg·mL^{-1} of catalyst. The pH of the solution has a vital role for degradation of phenolic compounds. The pH is the most important factor affecting the photocatalytic degradation process. The effect of pH on the degradation of 4-NP is illustrated in Figure S7. The experiments are performed at pH values of 4, 6, 8, and 10 by using composite mesoporous Co_3O_4−CuO NFs. At pH 6, the degradation of 4-NP was maximum, nearly 100%, and the percentage of degradation gradually decreases as the pH increases from 6 to 10. This can be explained on the basis of the pK_a value of 4-NP. The pK_a value of 4-NP is 7.15. At the pH > pK_a, the 4-NP dissociates; hence at the higher pH degradation decreases due to ionization of 4-NP molecules that leads to less photocatalytic degradation, while at acidic pH 6, the percentage of removal was higher because 4-NP is present in its undissociated state and the dispersion interaction predominates. Not merely 4-NP, the degradation percentage of 4-CP and phenol was higher at pH 6 due to the similar reasons as described above. In order to check the highly reactive composite Co_3O_4−CuO NFs having different Co and Cu ratios, the 4-NP degradation at pH 6 occurred in composite Co_3O_4−CuO NFs in the ratios Co:Cu = 1/4 (Co_3O_4−CuO NFs), Co:Cu = 1/3 (Co_3O_4−CuO NFs), and Co:Cu = 1/2 (Co_3O_4−CuO NFs). The highest degradation (100%) of 4-NP observed in composite Co_3O_4−CuO NFs is shown in Table S2. The degradation of composite Co_3O_4−CuO NFs is highest due to the high surface area (Table S2) as compared to other Co:Cu = 1/3 and Co:Cu = 1/2. This is due to high surface area providing high active sites support for 4-NP degradation. Hence, the composite Co_3O_4−CuO NFs is the optimum system for the photocatalytic phenolic compound degradation.

The photocatalytic degradation of phenolic compounds such as 4-NP, 4-CP, and phenol by different mesoporous NFs is shown in Figure 9. The reaction is carried out in the presence of visible light at pH 6 for 70 min. The intensity of UV−visible absorbance spectra of 4-NP decreases gradually from mesoporous Co_3O_4 NFs to composite Co_3O_4−CuO NFs as compared to standard 4-NP. The least absorbance intensity of mesoporous composite Co_3O_4−CuO NFs indicates high degradation of 4-NP by mesoporous composite Co_3O_4−CuO NFs (Figure 9a). The 4-NP color changes after degradation by different photocatalysts are pictured in Figure 9a (inset). The high degradation activity of 4-NP by mesoporous composite Co_3O_4−CuO NFs is due to the efficient visible light absorption and electron−hole separation properties. The efficient visible light absorption is due to the quantum confinement effect and electron−hole separation. Not only 4-NP degradation but the degradation of the 4-CP and phenol (Figure 9b,c) by different photocatalysts follows the same trend: mesoporous Co_3O_4NFs < CuO NFs < composite Co_3O_4−CuO NFs. But the % of degradation of 4-NP, 4-CP, and phenol varies with different photocatalysts (Table S3). The 4-NP has high % degradation as compared to 4-CP and phenol. This is due to the yellowish color of the 4-NP absorbing visible light more efficiently as compared to the colorless 4-CP and phenol.

The kinetics of phenolic compounds such as 4-NP, 4-CP, and phenol degradation by photocatalytic process on mesoporous composite Co_3O_4−CuO NFs is shown in parts d, e, and f of Figure 9, respectively. The results are plotted as

DOI: 10.1021/acsami.7b09026
ACS Appl. Mater. Interfaces 2017, 9, 35757−35774

log C_0/C vs t. The kinetic study was performed by varying the concentration of phenolic compounds (20, 30, and 40 mg·L^{-1}) with time (20, 40, and 60 min). With increase in the concentration of phenolic compounds, the degradation decreases. A linear relationship is observed between concentration of phenolic compounds and irradiation time. The photocatalytic degradation of phenolic compounds follows first order kinetics. The data are fitted to the first order rate model and the equations are given below.

$$\log \frac{C_0}{C} = Kt/2.303$$

$$K = \left(\log \frac{C_0}{C} \times 2.303\right)/t$$

where K is the first order rate constant, C_0 is the initial concentration of phenolic compounds, and C is the concentration at time t.

Trapping experiment has been performed in order to check the active species involve in the photocatalytic phenolic compounds degradation, in which the results were given in the Figure S8. For the trapping reaction, mesoporous composite Co_3O_4−CuO NFs is used as a photocatalyst for the degradation of the 4-NP. It has been well-known that the photogenerated holes (h^+), hydroxyl radicals ($^{\bullet}OH$), and superoxide radicals ($O_2^{\bullet-}$) are treated as the vital reactive species involved in photodegradation reactions. It is seen that when IPA is used as scavenger, 4-NP degradation decreased less as compared to reaction performed without scavenger, indicating involvement of $^{\bullet}OH$ species in the overall degradation process. The 4-NP degradation is significant when BQ is used as $O_2^{\bullet-}$ scavanger, which indicates the involvement of species $O_2^{\bullet-}$ in the reaction. In the Figure S8, the roles of both $O_2^{\bullet-}$ and $^{\bullet}OH$ are a little different for the degradation of the 4-NP. Moreover, the photocatalytic degradation of 4-NP decreased drastically when KI is used as scavenger. That means the photogenerated holes (h^+) are the major reactive species for the degradation of 4-NP. Conclusively, h^+, $O_2^{\bullet-}$, and $^{\bullet}OH$ species play an important role for the degradation of 4-NP in visible light. The high involvement of h^+ in the reaction media indicates effective separation of photogenerated electron and hole. The trapping reaction supports the role of CuO as a cocatalyst.

To check the complete mineralization of 4-NP after degradation, the FTIR spectra of pure mesoporous composite Co_3O_4−CuO NFs, composite Co_3O_4−CuO NFs (after degradation), and pure 4-NP have been examined (Figure S9). The signature peaks at 1340 and 1495 cm^{-1} are due the symmetric and asymmetric −NO_2 stretching vibration of 4-NP. The peaks at 1610 and 1590 cm^{-1} correspond to the C═C valence and arene structure, respectively. The peak at 3332 cm^{-1} is due to the O−H valence supperimposed by C−H valence. The signature peaks of 4-NP are absent in mesoporous composite Co_3O_4−CuO NFs after degradation, indicating the complete mineralization of 4-NP during reaction. The FTIR spectrum of pure mesoporous composite Co_3O_4−CuO NFs is shown in Figure S9 for comparison.

The stability study regarding 4-NP degradation by mesoporous composite Co_3O_4−CuO NFs is shown in Figure S10. The degradation reaction is evaluated by performing recycling experiments of 4-NP in similar conditions. The activity is found to be almost the same in three repeated runs, and then there is a slight decrease in the activity. The slight decrease of the activity (4th run) may be due to little structural deviation in the composites Co_3O_4−CuO NFs which is proved by the SEM study after the fourth run (Figure S11a). The XRD of composite Co_3O_4−CuO NFs after the fourth run of 4-NP degradation is shown in the Figure S11b. A similar XRD result is obtained in the cases of raw composite Co_3O_4−CuO NFs (Figure 1b) and used composite Co_3O_4−CuO NFs (after the fourth run of 4-NP degradation). Conclusively, the FTIR and recycling experiment proves the complete mineralization of the 4-NP, whereas the SEM and XRD study (after 4-NP degradation) proves the stability of the photocatalyst mesoporous composite Co_3O_4−CuO NFs in visible light.

In order to check the morphological effect on 4-NP degradation, three kinds of composite Co_3O_4−CuO have been tested. These are mesoporous composite Co_3O_4−CuO NFs, composite Co_3O_4−CuO NPs, and composite Co_3O_4−CuO bulk. The synthesis procedue of composite Co_3O_4−CuO NPs and composite Co_3O_4−CuO bulk is given in the Supporting Information, and the morphologies are shown in the Figure S12a,b. Figure S12a shows the perfect NPs morphology of the Co_3O_4−CuO NPs, whereas Figure S12b shows the random bulk morphology of the Co_3O_4−CuO bulk. It has been observed that mesoporous composite Co_3O_4−CuO NFs have high percentage of 4-NP degradation (100%) as compared to composite Co_3O_4−CuO NPs and Co_3O_4−CuO bulk (Table S4). Hence, it is well understood that mesoporosity and NPs within NFs morphology have greater advantage over NPs and bulk. This is because in the case of mesoporous composite Co_3O_4−CuO NFs, mesoporosity gives surface active property, NPs provide quantum confinement and high surface-to-volume ratio, and NFs increase the morphological stability. The composite Co_3O_4−CuO NPs with only high surface-to-volume ratio property resulted in 55% 4-NP degradation. The Co_3O_4−CuO bulk lacks all surface active properties, which is why it shows the least 4-NP degradation (20%).

3.7.1. Mechanism of Phenolic Compounds Degradation by Mesoporous Composite Co_3O_4−CuO NFs. Suitable conduction band (CB) and valence band level of the individual semiconductors are necessary for making a suitable photocatalyst. From the Mott−Schottky plot, it is calculated that the E_{fb} for Co_3O_4 NFs is 0.57 V (Figure 8c) which is approximately similar to the valence band potential (E_{VB}) of the Co_3O_4 NFs.[67] So the E_{VB} of Co_3O_4 NFs is 0.57 eV. From the UV−visible absorption spectrum, it is calculated that the band gap energy of the Co_3O_4 NFs is 2.01 eV (Figure 5c). Hence, the conduction band potential (E_{CB}) will be −1.44 eV. The band edge diagram of semiconductor Co_3O_4 is shown in the Scheme 3. After visible light irradiation, the photogenerated electron (e^-) and hole (h^+) are formed. The h^+ and e^- are utilized for the oxidation (^-OH) and reduction (O_2), respectively. But for photocatalytic system, electron and hole recombination retards the reaction efficiency. In order to solve the problem, a cocatalyst CuO is constructed that enables reduction of the e^- and h^+ recombination. Katsumata et al. have observed that CuO has four electron reduction ability.[71] The high reducing nature of CuO reduces Cu(II) to Cu(I) by trapping extra electrons from the semiconductor Co_3O_4. This phenomenon helps to suppress the electron−holes recombination and makes CuO an effective cocatalyst. This is the vital reason that mesoporous composite Co_3O_4−CuO NFs show higher phenolic compounds degradation in visible light as compared to other NFs (Figure 9). The degradation mechanism of phenolic compounds occurrs by the influence of electron and hole (Scheme 3).

DOI: 10.1021/acsami.7b09026
ACS Appl. Mater. Interfaces 2017, 9, 35757−35774

Scheme 3. Charge Separation and Electron−Hole Transfer in the Mesoporous Composite Co_3O_4−CuO NFs and Possible Reaction Mechanism

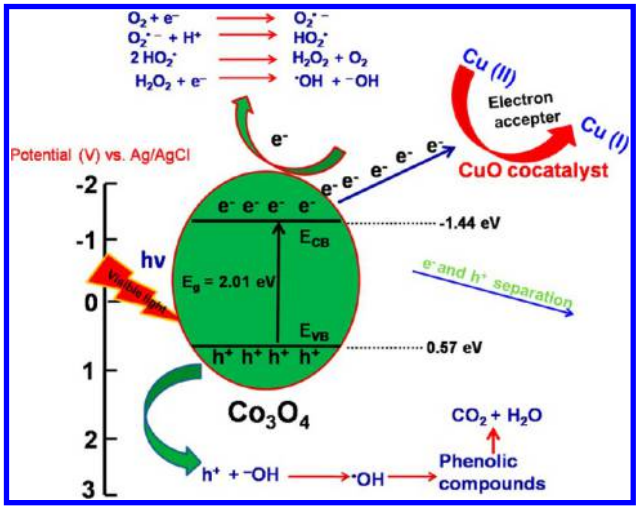

The photogenerated electrons are reacting with surface molecular oxygen generating active species such as $O_2^{\bullet-}$, $HO_2^{\bullet-}$, and $^{\bullet}OH$. These oxidizing species are responsible for oxidizing/decomposing the phenolic compounds. Another way, the most reactive $^{\bullet}OH$ radical is formed when the hole is reacting with ^{-}OH, which leads to oxidation/decomposistion of the phenolic compounds, resulting in degradation products CO_2 and H_2O. Thus, the charge separation and degradation mechanism have been well established in visible light.

3.7.2. Factor Affecting the Photocatalytic Activity. The photocatalytic degradation of phenolic compounds has been achieved by (a) the role of surface and textural properties which includes mesoporosity, surface hydroxyl group, NPs within NFs, and reactive facets, (b) quantum confinement and charge transfer phenomena, (c) lowering of electron−hole recombination and of oxygen vacancies, (c) role of cocatalyst, and (d) role of electrochemical study.

3.7.2.1. Mesoporosity, Surface Hydroxyl Group, NPs within NFs, and Reactive Facets. Mesoporous nanofibers have great deal of importance in the field of photocatalysis. These properties of materials help to increase the active site for the accommodation of a reacting molecule. It has already been examined that all mesoporous NFs show mesoporosity (Figure 1). Of the textural properties such as surface area, pore volume, and pore diameter, the mesoporous composite Co_3O_4−CuO NFs have high surface area as compared to CO_3O_4 NFs and CuO NFs (Table S1), resulting in high photocatalytic phenolic compounds degradation compared with other NFs. This is due to the high interaction between the phenolic compounds with surface reactive sites of the mesoporous composite Co_3O_4−CuO NFs. Another factor is the role of particle size with the NFs. If the particle is small, i.e., below 100 nm (nanoparticles), it will act as an efficient photocatalyst because of high surface to volume ratio. Generally, the surface area increases with decreasing particle size, and if the surface area is more, then the availability of the active site will be more, leading to an increase in the catalytic activity. It has been seen from TEM studies (Figures 3 and 4) that the NPs are present within all NFs. Table S1 shows that all mesoporous NFs exhibit small size NPs, resulting in high phenolic compounds degradation in visible light. Among all mesoporous NFs, mesoporous composite Co_3O_4−CuO NFs have high degradation activity. This is due to the small size NPs as compared to other NFs. Surface hydroxyl groups have high impact for an efficient photocatalytic application.[72] This is because surface hydroxyl groups are creating more $^{\bullet}OH$ radicals for the photocatalytic application.[73] Presently, from the XPS study of O 1s core-level spectrum (Figure 7), the presence of the surface hydroxyl groups in the mesoporous composite Co_3O_4−CuO NFs is proved. The generated $^{\bullet}OH$ radicals from the surface hydroxyl groups enhanced the phenolic compounds degradation. Recently, Ma et al. and Su et al. investigated the exposed reactive facets of the {110} and {001} for Co_3O_4 and CuO, respectively.[21,28] In the present study, the FFT image (HR-TEM study) of the Co_3O_4 and CuO showing the {110} and {001} completely matched the result from Ma et al. and Su et al. Hence, the enhanced degradation activity is also due to the exposed reacting facets of the mesoporous Co_3O_4, CuO, and composite Co_3O_4−CuO NFs. Conclusively, the mesoporosity, surface hydroxyl group, NPs within NFs, and reactive facets have great role in the enhancement of the phenolic compounds degradation by mesoporous Co_3O_4, CuO, and composite Co_3O_4−CuO NFs.

3.7.2.2. Lowering of Electron−Hole Recombination and Oxygen Vacancies. The PL intensities of the mesoporous composite Co_3O_4−CuO NFs are the lowest as compared to mesoporous Co_3O_4 NFs and CuO NFs. Generally, the PL emission describes the recombination of excited electrons and holes under light irradation. Hence, the lower PL intensity indicates a lower recombination rate of electron−hole.[74] The highest photocatalytic activity is directly proportional to the lowest recombination of electron−hole. The Schottky barrier appears to be due to the mixing of the CuO into the Co_3O_4 in mesoporous composite Co_3O_4−CuO NFs, resulting in lowering of electron−hole recombination as compared to Co_3O_4 and CuO NFs. Hence, the lowest electron−hole recombination of mesoporous composite Co_3O_4−CuO NFs indicates the highest photocatalytic degradation of phenolic compounds in visible light. It has been observed that oxygen vacancies help to enhance the photocatalytic application by trapping the electrons, resulting in suppression of the electron−hole recombination.[75] Hence, in the present study, the oxygen vacancies present in the mesoporous composite Co_3O_4−CuO NFs could act as an electron trapping center, which may be responsible for an efficient degradation activity.

3.7.2.3. Quantum Confinement and Charge Transfer Phenomena. Quantum confinement phenomena enhance light absorption property and quick transpport of photogenerated electrons and holes. Quantum confined effect favors higher rates of interfacial charge transfer.[48] This phenomenon favors the high photocatalytic activity.[76] The quantum confinement phenomena of mesoporus Co_3O_4 NFs, CuO NFs, and composite Co_3O_4−CuO NFs have been examined by SERS, UV−visible absorption spectroscopy, UV−visible−NIR DRS spectroscopy, and PL spectra. Quantum confinement arose because of the small NPs present within the aforesaid NFs. Due to quantum confinement phenomena, all three NFs show high photodegradation of phenolic compounds in visible light. Among them, mesoporous composite Co_3O_4−CuO NFs show high degradation activity than others. This is due to the small size NPs of Co_3O_4−CuO NFs, which enables harvesting of more light through quantum confinement phenomena. It has been reported that interparticle transfer of charge carriers contributes to the enhanced photocatalytic efficiency.[77] The

DOI: 10.1021/acsami.7b09026
ACS Appl. Mater. Interfaces 2017, 9, 35757−35774

charge transfer transition favors an internal oxidation−reduction process which facilitates photocatalysis in the visible region. The mesoporous composite Co_3O_4−CuO NFs show high degradation activity which is due to the internal charge transfer between Co^{2+}, Co^{3+}, and Cu^{2+}.

3.7.2.4. Role of CuO as Cocatalyst in Mesoporous Composite Co_3O_4−CuO NFs. The lowest PL spectrum (Figure 6) of mesoporous composite Co_3O_4−CuO NFs as compared to neat Co_3O_4 NFs and CuO NFs proves the presence of CuO as cocatalyst. That is the vital reason that mesoporous composite Co_3O_4−CuO NFs show higher phenolic compounds degradation than neat Co_3O_4 NFs and CuO NFs. As a cocatalyst, CuO enhances the photocatalytic activity of mesoporous composite Co_3O_4−CuO NFs by (i) absorbing the photoexcited electrons, as an electron acceptor, which leads to high suppresion of electron−hole recombination. The lowering of electron−hole recombination increases the photocatalytic phenolic compounds degradation. It has been reported that Cu(II) species in nanoclusters are very efficient photocatalyst in visible light.[78] (ii) Enhancement is also done by trapping of electrons by Cu(II) center of CuO and reduction to Cu(I) in composite Co_3O_4−CuO NFs. This process is also helps to suppress the electron−hole recombination and enhanced the phenolic compounds degradation.

3.7.2.5. Role of Electrochemical Study. The electrochemical study favors the high phenolic compounds degradation by mesoporous composite Co_3O_4−CuO NFs as compared to the neat mesoporous Co_3O_4 NFs and CuO NFs. The generation of high current density from the composite Co_3O_4−CuO NFs favors the high photocatalytic degradation through harvesting of electrons and holes. The high E_{fb} value of the composite Co_3O_4−CuO NFs as compared to neat NFs suppresses electron−hole recombination and hence increases the photocatalytic degradation of the phenolic compounds. From EIS study, a lower value of R_{ct} and smaller value of W_s in composite Co_3O_4−CuO NFs as compared to neat NFs support the high phenolic compound degradation through charge transfer, separation of electron−hole by CuO as cocatalyst, and ion movement.

4. CONCLUSION

Here, fabrication of electrospun mesoporous Co_3O_4 NFs, CuO NFs, and composite Co_3O_4−CuO NFs was performed by using a mixed PVP/PEG polymeric template. Design and reaction of NPs and mesoporosity within NFs are a vital achivement in the present study. The mesoporosity provides the high surface area whereas NPs provide quantum confinement phenomena, which is the significance of the present investigation. The generation of the quantum confinement effect is well-established and proved by enhancing SERS signals, red shifting from optical study and blue shifting from PL study. It has been examined that mesoporos composite Co_3O_4−CuO NFs show higher photocatalytic activity for degradation of phenolic compounds under visible light as compared to mesoporous Co_3O_4 and CuO NFs. The photocatalyst mesoporous composite Co_3O_4−CuO NFs are stable up to fourth runs and there is minimal change in degradation activity, proved by stability test. The FTIR study proves the complete mineralization of the 4-NP. That means the photocatalyst will be stable, reactive, and reusable for multiple runs. The high photocatalytic activity by mesoporous composite Co_3O_4−CuO NFs is ascribed to the role of low cost CuO as cocatalyst in visible light. The suggested CuO as cocatalyst is proved by the lowest PL intensity in the composite Co_3O_4−CuO NFs which conclude that CuO acts as an electron sink/trapper, resulting in an efficient electron−hole separation. Moreover, quantum confinement phenomena from NPs within NFs, provide high visible light absorption property which enhances the degradation activity. That is the main reason that all fabricated mesoporous NFs have good degradation activity. Mesoporosity with NFs increases the surface reactivity for an efficient photodegradation of the phenolic compounds. Oxygen vacancies within NFs help to enhance the photocatalytic activity by separating electron−hole. The electrochemical properties of the mesoporous NFs support the high photocatalytic activity and prove the role of CuO as cocatalyst. Internal charge transfer phenomena between Co^{2+}, Co^{3+}, and Cu^{2+} and exposed reactive facets {110} for Co_3O_4 and {001} are also helpful for harvesting visible light effficiently for photocatalytic application. The aforesaid factors within mesoporous NFs are responsible for an efficient photocatalytic degradation of phenolic compounds under visible light.

■ ASSOCIATED CONTENT

Supporting Information

The Supporting Information is available free of charge on the ACS Publications website at DOI: 10.1021/acsami.7b09026.

Table summarizing textural properties of mesoporous NFs, SEM picture of electrospun porous CuO nanoflowers, HR-TEM micrographs of mesoporous Co_3O_4 NFs and CuO NFs, STEM−EDX spectra of mesoporous NFs, UV−vis−NIR DRS FTIR spectra of mesoporous NFs, Raman spectra of all mesoporous NFs, effect of pH, table summarizing % of phenolic compound degradation, trapping experiment, 4-NP degradation, and recycling study (PDF)

■ AUTHOR INFORMATION

Corresponding Authors

*A.C.P.: e-mail, pradhan@unam.bilkent.edu.tr.

*T.U.: e-mail, tamer@unam.bilkent.edu.tr.

ORCID

Tamer Uyar: 0000-0002-3989-4481

Author Contributions

A.C.P has conducted the experiments, and A.C.P and T.U have both contributed to the writing of the manuscript. All authors have given approval to the final version of the manuscript.

Funding

A.C.P. acknowledges the Scientific & Technological Research Council of Turkey (TUBITAK), BIDEB 2216 Fellowships for an International Postdoctoral Researcher. T.U. acknowledges the Turkish Academy of Sciences—Outstanding Young Scientists Award Program (TUBA-GEBIP), Turkey, for partial funding.

Notes

The authors declare no competing financial interest.

■ ACKNOWLEDGMENTS

Authors thank M. Guler for TEM−STEM technical support.

■ REFERENCES

(1) Zhang, S.; Gao, H.; Liu, X.; Huang, Y.; Xu, X.; Alharbi, N. S.; Hayat, T.; Li, J. Hybrid 0D-2D Nanoheterostructures: In Situ Growth of Amorphous Silver Silicates Dots on g-C_3N_4 Nanosheets for Full-

Spectrum Photocatalysis. *ACS Appl. Mater. Interfaces* **2016**, *8*, 35138−35149.
(2) Zhang, S.; Yang, H.; Gao, H.; Cao, R.; Huang, J.; Xu, X. One-pot Synthesis of CdS Irregular Nanospheres Hybridized with Oxygen-Incorporated Defect-Rich MoS_2 Ultrathin Nanosheets for Efficient Photocatalytic Hydrogen Evolution. *ACS Appl. Mater. Interfaces* **2017**, *9*, 23635−23646.
(3) Pradhan, A. C.; Nanda, B.; Parida, K. M.; Rao, G. R. Fabrication of the Mesoporous Fe@MnO_2NPs−MCM-41 Nanocomposite: An Efficient Photocatalyst for Rapid Degradation of Phenolic Compounds. *J. Phys. Chem. C* **2015**, *119*, 14145−14159.
(4) Pradhan, A. C.; Nanda, B.; Parida, K. M.; Das, M. Quick Photo-Fenton Degradation of Phenolic Compounds by Cu/Al_2O_3−MCM-41 Under Visible Light Irradiation: Small Particle Size, Stabilization of Copper, Easy Reducibility of Cu and Visible Light Active Material. *Dalton Trans.* **2013**, *42*, 558−566.
(5) Kung, K. H.; McBride, M. B. Bonding of Chlorophenols on Iron and Aluminum Oxides. *Environ. Sci. Technol.* **1991**, *25*, 702−709.
(6) Pradhan, A. C.; Sahoo, M. K.; Bellamkonda, S.; Parida, K. M.; Rao, G. R. Enhanced Photodegradation of Dyes and Mixed Dyes by Heterogeneous Mesoporous Co−Fe/Al_2O_3− MCM-41 Nanocomposites: Nanoparticles formation, Semiconductor Behavior and Mesoporosity. *RSC Adv.* **2016**, *6*, 94263−94277.
(7) Kayaci, F.; Vempati, S.; Ozgit-Akgun, C.; Biyikli, N.; Uyar, T. Enhanced Photocatalytic Activity of Homoassembled ZnO Nanostructures on Electrospun Polymeric Nanofibres: A Combination of Atomic Layer Deposition and Hydrothermal Growth. *Appl. Catal., B* **2014**, *156−157*, 173−183.
(8) Kayaci, F.; Ozgit-Akgun, C.; Donmez, I.; Biyikli, N.; Uyar, T. Polymer-Inorganic Core-Shell Nanofibers by Electrospinning and Atomic Layer Deposition: Flexible Nylon-ZnO Core-Shell Nanofiber Mats and Their Photocatalytic Activity. *ACS Appl. Mater. Interfaces* **2012**, *4* (11), 6185−6194.
(9) Kayaci, F.; Vempati, S.; Ozgit-Akgun, C.; Donmez, I.; Biyikli, N.; Uyar, T. Selective Isolation of Electron or Hole in Photocatalysis: ZnO-TiO_2 and TiO_2-ZnO Core-Shell Structured Heterojunction Nanofibers via Electrospinning and Atomic Layer Deposition. *Nanoscale* **2014**, *6*, 5735−5745.
(10) Vinu, R.; Madras, G. Kinetics of Simultaneous Photocatalytic Degradation of Phenolic Compounds and Reduction of Metal Ions with Nano-TiO_2. *Environ. Sci. Technol.* **2008**, *42*, 913−919.
(11) Kayaci, F.; Vempati, S.; Ozgit-Akgun, C.; Donmez, I.; Biyikli, N.; Uyar, T. Transformation of Polymer-ZnO Core-Shell Nanofibers into ZnO Hollow Nanofibers: Intrinsic Defect Reorganization in ZnO and its Influence on the Photocatalysis. *Appl. Catal., B* **2015**, *176−177*, 646−653.
(12) Senthamizhan, A.; Balusamy, B.; Aytac, Z.; Uyar, T. Grain Boundary Engineering in Electrospun ZnO Nanostructures as Promising Photocatalysts. *CrystEngComm* **2016**, *18*, 6341−6351.
(13) Farhadi, S.; Pourzare, K.; Bazgir, S. Co_3O_4 Nanoplates: Synthesis, Characterization and Study of Optical and Magnetic Properties. *J. Alloys Compd.* **2014**, *587*, 632−637.
(14) Chang, X.; Wang, T.; Zhang, P.; Zhang, J.; Li, A.; Gong, J. Enhanced Surface Reaction Kinetics and Charge Separation of p−n Heterojunction Co_3O_4/BiVO4 Photoanodes. *J. Am. Chem. Soc.* **2015**, *137*, 8356−8359.
(15) Zhang, L.; Gao, Z.; Liu, C.; Zhang, Y.; Tu, Z.; Yang, X.; Yang, F.; Wen, Z.; Zhu, L.; Liu, R.; Li, Y.; Cui, L. Synthesis of TiO_2 Decorated Co_3O_4 Acicular Nanowire Arrays and Their Application as an Ethanol Sensor. *J. Mater. Chem. A* **2015**, *3*, 2794−2801.
(16) Wu, Y.; Ma, M.; Zhang, B.; Gao, Y.; Lu, W.; Guo, Y. Controlled Synthesis of Porous Co_3O_4 Nanofibers by Spiral Electrospinning and Their Application for Formaldehyde Oxidation. *RSC Adv.* **2016**, *6*, 102127−102133.
(17) Yang, J.; Wang, D.; Han, H.; Li, C. Roles of Cocatalysts in Photocatalysis and Photoelectrocatalysis. *Acc. Chem. Res.* **2013**, *46*, 1900−1909.
(18) Shah, Z. H.; Wang, J.; Ge, Y.; Wang, C.; Mao, W.; Zhang, S.; Lu, R. Highly enhanced plasmonic photocatalytic activity of Ag/AgCl/TiO_2 by CuO Co-catalyst. *J. Mater. Chem. A* **2015**, *3*, 3568−3575.
(19) Arai, T.; Horiguchi, M.; Yanagida, M.; Gunji, T.; Sugihara, H.; Sayama, K. Reaction Mechanism and Activity of WO_3-Catalyzed Photodegradation of Organic Substances Promoted by a CuO Cocatalyst. *J. Phys. Chem. C* **2009**, *113*, 6602−6609.
(20) Nanda, B.; Pradhan, A. C.; Parida, K. M. A Comparative Study on Adsorption and Photocatalytic Dye Degradation under Visible Light Irradiation by Mesoporous MnO_2 Modified MCM-41 Nanocomposite. *Microporous Mesoporous Mater.* **2016**, *226*, 229−242.
(21) Ma, C. Y.; Mu, Z.; Li, J. J.; Jin, Y. G.; Cheng, J.; Lu, G. Q.; Hao, Z. P.; Qiao, S. Z. Mesoporous Co_3O_4 and Au/Co_3O_4 Catalysts for Low-Temperature Oxidation of Trace Ethylene. *J. Am. Chem. Soc.* **2010**, *132*, 2608−2613.
(22) Wessel, C.; Ostermann, R.; Dersch, R.; Smarsly, B. M. Formation of Inorganic Nanofibers from Preformed TiO_2 Nanoparticles via Electrospinning. *J. Phys. Chem. C* **2011**, *115*, 362−372.
(23) Zhan, S.; Chen, D.; Jiao, X.; Tao, C. Long TiO_2 Hollow Fibers with Mesoporous Walls: Sol-Gel Combined Electrospun Fabrication and Photocatalytic Properties. *J. Phys. Chem. B* **2006**, *110*, 11199−11204.
(24) Tanaka, K.; Capule, F. V. M; Hisanaga, T. Effect of Crystallinity of TiO_2 on its Photocatalytic action. *Chem. Phys. Lett.* **1991**, *187*, 73−76.
(25) Alivisatos, A. P. Semiconductor Clusters, Nanocrystals, and Quantum Dots. *Science* **1996**, *271*, 933−937.
(26) Ma, C. Y.; Mu, Z.; Li, J. J.; Jin, Y. G.; Cheng, J.; Lu, G. Q.; Hao, Z. P.; Qiao, S. Z. Mesoporous Co_3O_4 and Au/Co_3O_4 Catalysts for Low-Temperature Oxidation of Trace Ethylene. *J. Am. Chem. Soc.* **2010**, *132*, 2608−2613.
(27) Xie, X.; Li, Y.; Liu, Z.-Q.; Haruta, M.; Shen, W. Low-temperature Oxidation of CO Catalysed by Co_3O_4 Nanorods. *Nature* **2009**, *458*, 746−749.
(28) Su, D.; Xie, X.; Dou, S.; Wang, G. CuO Single Crystal with Exposed {001} facets - A Highly Efficient Material for Gas Sensing and Li-ion Battery Applications. *Sci. Rep.* **2015**, *4* (5753), 1−9.
(29) Zhang, Y. X.; Zheng, J.; Gao, G.; Kong, Y. F.; Zhi, X.; Wang, K.; Zhang, X. Q.; Cui, D. X. Biosynthesis of Gold Nanoparticles Using Chloroplasts. *Int. J. Nanomed.* **2011**, *6*, 2899−2906.
(30) Shi, Y.; Yang, Z.; Liu, Y.; Yu, J.; Wang, F.; Tong, J.; Su, B.; Wang, Q. Fabricating a g-C_3N_4/CuOx Heterostructure with Tunable Valence Transition for Enhanced Photocatalytic Activity. *RSC Adv.* **2016**, *6*, 39774−39783.
(31) Sing, K. S. W.; Everett, D. H.; Haul, R. A. W.; Moscou, L.; Pierotti, R. A.; Rouquerol, J.; Siemieniewska, T. Reporting Physisorption Data for Gas/Solid Systems with Special Reference to the Determination of Surface area and Porosity. *Pure Appl. Chem.* **1985**, *57*, 603−619.
(32) Goyne, K. W.; Zimmerman, A. R.; Newalkar, B. L.; Komarneni, S.; Brantley, S. L.; Chorover, J. Surface Charge of Variable Porosity Al_2O_3(s) and SiO_2(s) Adsorbents. *J. Porous Mater.* **2002**, *9*, 243−256.
(33) Tanev, P. T.; Pinnavaia, T. J. Mesoporous Silica Molecular Sieves Prepared by Ionic and Neutral Surfactant Templating: A Comparison of Physical Properties. *Chem. Mater.* **1996**, *8*, 2068−2070.
(34) Zhang, L.; Gao, Z.; Liu, C.; Zhang, Y.; Tu, Z.; Yang, X.; Yang, F.; Wen, Z.; Zhu, L.; Liu, R.; Li, Y.; Cui, L. Synthesis of TiO_2 Decorated Co_3O_4 Acicular Nanowire Arrays and Their Application as an Ethanol Sensor. *J. Mater. Chem. A* **2015**, *3*, 2794−2801.
(35) Deng, J.; Wang, L.; Lou, Z.; Zhang, T. Design of CuO−TiO_2 Heterostructure Nanofibers and Their Sensing Performance. *J. Mater. Chem. A* **2014**, *2*, 9030−9034.
(36) Yamamoto, T.; Tanaka, T.; Kuma, R.; Suzuki, S.; Amano, F.; Shimooka, Y.; Kohno, Y.; Funabiki, T.; Yoshida, S. NO Reduction with CO in the Presence of O_2 Over Al_2O_3-Supported and Cu-Based Catalysts. *Phys. Chem. Chem. Phys.* **2002**, *4*, 2449−2458.
(37) Liu, H.; Patzke, G. R. Visible-Light-Driven Water Oxidation with Nanoscale Co_3O_4: New Optimization Strategies. *Chem. - Asian J.* **2014**, *9*, 2249−2259.

DOI: 10.1021/acsami.7b09026
ACS Appl. Mater. Interfaces 2017, 9, 35757−35774

(38) Cao, J.; Xu, B.; Lin, H.; Luo, B.; Chen, S. Novel Heterostructured Bi_2S_3/BiOI Photocatalyst: Facile Preparation, Characterization and Visible Light Photocatalytic Performance. *Dalton Trans.* **2012**, *41*, 11482−11490.
(39) Siddiqui, H.; Qureshi, M. S.; Haque, F. Z. One-step, Template-Free Hydrothermal Synthesis of CuO Tetrapods. *Optik* **2014**, *125*, 4663−4667.
(40) Haque, F. Z.; Parra, M. R.; Siddiqui, H.; Singh, N.; Singh, N.; Pandey, P.; Mishra, K. M. PVP Assisted Shape-Controlled Synthesis of Self-Assembled 1D ZnO and 3D CuO Nanostructures. *Opt. Spectrosc.* **2016**, *120*, 408−414.
(41) Zhang, N.; Shi, J.; Mao, S. S.; Guo, L. Co_3O_4 Quantum Dots: Reverse Micelle Synthesis and Visible-Light-Driven Photocatalytic Overall Water Splitting. *Chem. Commun.* **2014**, *50*, 2002−2004.
(42) de Julián Fernández, C. J.; Mattei, G.; Sada, C.; Battaglin, C.; Mazzoldi, P. Nanostructural and Optical Properties of Cobalt and Nickel−Oxide/Silica Nanocomposites. *Mater. Sci. Eng., C* **2006**, *26*, 987−991.
(43) Shimizu, K.; Maeshima, H.; Satsuma, A.; Hattori, T. Transition Metal-Aluminate Catalysts for NO Reduction by C_3H_6. *Appl. Catal., B* **1998**, *18*, 163−170.
(44) Erdogan, I. Y.; Gullu, O. Optical and Structural Properties of CuO Nanofilm: Its diode application. *J. Alloys Compd.* **2010**, *492*, 378−383.
(45) Kumar, P. S.; Selvakumar, M.; Babu, S. G.; Jaganathan, S. K.; Karuthapandian, S.; Chattopadhyay, S. Novel CuO/Chitosan Nanocomposite thin film: Facile Hand-Picking Recoverable, Efficient and Reusable Heterogeneous Photocatalyst. *RSC Adv.* **2015**, *5*, 57493−57501.
(46) Wang, X.; Chen, X.; Gao, L.; Zheng, H.; Zhang, Z.; Qian, Y. One-Dimensional Arrays of Co_3O_4 Nanoparticles: Synthesis, Characterization, and Optical and Electrochemical Properties. *J. Phys. Chem. B* **2004**, *108*, 16401−16404.
(47) Bhaumik, A.; Shearin, A. M.; Patel, R.; Ghosh, K. Significant Enhancement of Optical Absorption Through Nano-Structuring of Copper Based Oxide Semiconductors: Possible Future Materials for Solar Energy Applications. *Phys. Chem. Chem. Phys.* **2014**, *16*, 11054−11066.
(48) Marcus, R. Chemical and Electrochemical Electron-Transfer Theory. *Annu. Rev. Phys. Chem.* **1964**, *15*, 155−196.
(49) Chethan, P. S.; Joshi, M. P.; Mohan, S. R.; Dhami, T. S.; Khatei, J.; Rao, K. S. K.; Kukreja, L. M.; Sanjeev, G. Effect of Electron Beam Irradiation on Photoluminescence Properties of Thioglycolic Acid (TGA) Capped CdTe Nanoparticles. *Adv. Mater. Lett.* **2013**, *4*, 454−457.
(50) Jinfeng, Z.; Yunguang, Y.; Wei, L. Preparation, Characterization, and Activity Evaluation of CuO/F-TiO_2 Photocatalyst. *Int. J. Photoenergy* **2012**, *2012*, 1−9.
(51) Hou, H.; Shang, M.; Gao, F.; Wang, L.; Liu, Q.; Zheng, J.; Yang, Z.; Yang, W. Highly Efficient Photocatalytic Hydrogen Evolution in Ternary Hybrid TiO_2/CuO/Cu Thoroughly Mesoporous Nanofibers. *ACS Appl. Mater. Interfaces* **2016**, *8*, 20128−20137.
(52) Li, G.; Dimitrijevic, N. M.; Chen, L.; Rajh, T.; Gray, K. A. Role of Surface/Interfacial Cu^{2+} Sites in the Photocatalytic Activity of Coupled CuO-TiO_2 Nanocomposites. *J. Phys. Chem. C* **2008**, *112*, 19040−19044.
(53) Naseri, A.; Samadi, M.; Mahmoodi, N. M.; Pourjavadi, A.; Mehdipour, H.; Moshfegh, A. Z. Tuning Composition of Electrospun ZnO/CuO Nanofibers: Toward Controllable and Efficient Solar Photocatalytic Degradation of Organic Pollutants. *J. Phys. Chem. C* **2017**, *121*, 3327−3338.
(54) Rakibuddin, Md.; Mandal, S.; Ananthakrishnan, R. A Novel Ternary CuO Decorated Ag_3AsO_4/GO Hybrid as a Z-scheme Photocatalyst for Enhanced Degradation of Phenol under Visible Light. *New J. Chem.* **2017**, *41*, 1380−1389.
(55) Ho, C.-T.; Weng, T.-H.; Wang, C.-Y.; Yen, S.-J.; Yew, T.-R. Tunable Band Gaps of $Co_{3-x}Cu_xO_4$ Nanorods with Various Cu Doping Concentrations. *RSC Adv.* **2014**, *4*, 20053−20057.
(56) Huang, H.; Zhu, W.; Tao, X.; Xia, Y.; Yu, Z.; Fang, J.; Gan, Y.; Zhang, W. Nanocrystal-Constructed Mesoporous Single-Crystalline Co_3O_4 Nanobelts with Superior Rate Capability for Advanced Lithium-Ion Batteries. *ACS Appl. Mater. Interfaces* **2012**, *4*, 5974−5980.
(57) Rakibuddin, Md.; Ananthakrishnan, R. Porous ZnO/Co_3O_4 Hetero Nanostructures Derived from Nano Coordination Polymers for Enhanced Gas Sorption and Visible Light Photocatalytic Applications. *RSC Adv.* **2015**, *5*, 68117−68127.
(58) Liu, Y.; Zhu, G.; Ge, B.; Zhou, H.; Yuan, A.; Shen, X. Concave Co_3O_4 Octahedral Mesocrystal: Polymer-Mediated Synthesis and Sensing Properties. *CrystEngComm* **2012**, *14*, 6264−6270.
(59) Usha, V.; Kalyanaraman, S.; Thangavel, R.; Vettumperumal, R. Effect of Catalysts on the Synthesis of CuO Nanoparticles: Structural and Optical Properties by Sol−Gel Method. *Superlattices Microstruct.* **2015**, *86*, 203−210.
(60) Foyer, C. H.; Halliwell, B. The Presence of Glutathione and Glutathione Reductase in Chloroplasts: A Proposed Role in Ascorbic Acid Metabolism. *Planta* **1976**, *133*, 21−25.
(61) Nie, S.; Emory, S. R. Probing Single Molecules and Single Nanoparticles by Surface-Enhanced Raman scattering. *Science* **1997**, *275*, 1102−1106.
(62) Lombardi, J. R.; Birke, R. L. A Unified View of Surface-Enhanced Raman Scattering. *Acc. Chem. Res.* **2009**, *42*, 734−742.
(63) Xue, X.; Ji, W.; Mao, Z.; Mao, H.; Wang, Y.; Wang, X.; Ruan, W.; Zhao, B.; Lombardi, J. R. Raman Investigation of Nanosized TiO_2: Effect of Crystallite Size and Quantum Confinement. *J. Phys. Chem. C* **2012**, *116*, 8792−8797.
(64) Liu, G. J.; Ye, S.; Yan, P. L.; Xiong, F. G.; Fu, P.; Wang, Z. L.; Chen, Z.; Shi, J. Y.; Li, C. Enabling an IntegratedTantalum Nitride Photoanode to Approach the TheoreticalPhotocurrent Limit for Solar Water Splitting. *Energy Environ. Sci.* **2016**, *9*, 1327−1334.
(65) Yang, Y.; Xu, D.; Wu, Q.; Diao, P. Cu_2O/CuO Bilayered Composite as a High-Efciency Photocathode for Photoelectrochemical Hydrogen Evolution Reaction. *Sci. Rep.* **2016**, *6* (35158), 1−13.
(66) Chua, C. S.; Ansovini, D.; Lee, C. J. J.; Teng, Y. T.; Ong, L. T.; Chi, D.; Hor, T. S. A.; Raja, R.; Lim, Y.-F. The Effect of Crystallinity on Photocatalytic Performance of Co_3O_4Water-Splitting Cocatalysts. *Phys. Chem. Chem. Phys.* **2016**, *18*, 5172−5178.
(67) Kandi, D.; Martha, S.; Thirumurugan, A.; Parida, K. M.Modification of BiOIMicroplates with CdS QDs for Enhancing Stability, Optical Property, Electronic Behavior toward Rhodamine B Decolorization, and Photocatalytic Hydrogen Evolution. *J. Phys. Chem. C* **2017**, *121*, 4834−4849.
(68) Chen, X.; Tang, B.; Luo, J.; Wan, Y. Towards High-Performance Polysulfone Membrane: The Role of PSF-b-PEG Copolymer additive. *Microporous Mesoporous Mater.* **2017**, *241*, 355−365.
(69) Hou, H.; Wang, L.; Gao, F.; Wei, G.; Tang, B.; Yang, W.; Wu, T. General Strategy for Fabricating Thoroughly Mesoporous Nanofibers. *J. Am. Chem. Soc.* **2014**, *136*, 16716−16719.
(70) Reverberi, A. P.; Salerno, M.; Lauciello, S.; Fabiano, B. Synthesis of Copper Nanoparticles in Ethylene Glycol by Chemical Reduction with Vanadium (+2) Salts. *Materials* **2016**, *9*, 809.
(71) Katsumata, H.; Oda, Y.; Kaneco, S.; Suzuki, T. Photocatalytic Activity of Ag/CuO/WO_3 under Visible Light Irradiation. *RSC Adv.* **2013**, *3*, 5028−5035.
(72) Wang, X.; Cao, L.; Chen, D.; Caruso, R. A. Engineering of Monodisperse Mesoporous Titania Beads for Photocatalytic Applications. *ACS Appl. Mater. Interfaces* **2013**, *5*, 9421−9428.
(73) Wu, C.-Y.; Tu, K.-J.; Deng, J.-P.; Lo, Y.-S.; Wu, C.-H. Markedly Enhanced Surface Hydroxyl Groups of TiO_2 Nanoparticles with Superior Water-Dispersibility for Photocatalysis. *Materials* **2017**, *10*, 566.
(74) Liu, K.; Su, C.-Y.; Perng, T.-P. Highly Porous N-Doped TiO_2 Hollow Fibers with Internal Three-Dimensional Interconnected Nanotubes for Photocatalytic Hydrogen Production. *RSC Adv.* **2015**, *5*, 88367−88374.

DOI: 10.1021/acsami.7b09026
ACS Appl. Mater. Interfaces 2017, 9, 35757−35774

(75) Zhang, Y.; Dai, R.; Hu, S. Study of the Role of Oxygen Vacancies as ActiveSites in Reduced Graphene Oxide-Modified TiO_2. *Phys. Chem. Chem. Phys.* **2017**, *19*, 7307−7315.
(76) Zhao, J.; Holmes, M. A.; Osterloh, F. E. Quantum Confinement Controls Photocatalysis: A Free Energy Analysis for Photocatalytic Proton Reduction at CdSe Nanocrystals. *ACS Nano* **2013**, *7*, 4316−4325.
(77) Li, G.; Dimitrijevic, N. M.; Chen, L.; Rajh, T.; Gray, K. A. Role of Surface/Interfacial Cu^{2+} Sites in the Photocatalytic Activity of Coupled CuO-TiO_2 Nanocomposites. *J. Phys. Chem. C* **2008**, *112*, 19040−19044.
(78) Qiu, X.; Miyauchi, M.; Sunada, K.; Minoshima, M.; Liu, M.; Lu, Y.; Li, D.; Shimodaira, Y.; Hosogi, Y.; Kuroda, Y.; Hashimoto, K. Hybrid Cu_xO/TiO_2 Nanocomposites As Risk-Reduction Materials in Indoor Environments. *ACS Nano* **2012**, *6*, 1609−1618.

DOI: 10.1021/acsami.7b09026
ACS Appl. Mater. Interfaces 2017, 9, 35757−35774